Solar Energy Materials & Solar Cells 295 (2026) 113925

Contents lists available at ScienceDirect

Solar Energy Materials and Solar Cells

journal homepage: www.elsevier.com/locate/solmat

Enhanced thermal models of photovoltaic modules by electrical operating conditions dependency

Giuseppe Marco Tina [a], Amr Osama [a,b,c,*], Antonio Gagliano [a], Gaetano Mannino [a], Francisco José Munoz-Rodríguez [d], Gabino Jiménez-Castillo [e]

[a] Department of Electric, Electronics and Computer Engineering, University of Catania, Viale Andrea Doria 6, Catania, 95125, Italy
[b] Department of Information and Electrical Engineering and Applied Mathematics (DIEM) – University of Salerno (UNISA), Via Giovanni Paolo II, 132, Fisciano, 84084, SA, Italy
[c] Mechanical Power Engineering Department, Faculty of Engineering, Port Said University, Port Fuad, Egypt
[d] Department of Electronic and Automatic Engineering, Universidad de Jaen, Jaen, 23071, Spain
[e] Department of Electrical Engineering, University of Jaen, Jaen, Spain

ARTICLE INFO

Keywords:
Thermal model
Photovoltaics
Module temperature
Sandia model
Faiman model
Electrical operating status

ABSTRACT

The increasing penetration of photovoltaic (PV) systems poses challenges to the reliability and adequacy of power systems. To support grid stability, PV systems must evolve to be capable of providing frequency regulation and reserve services—including not only down frequency reserve but also up reserve. This latter service requires PV modules to operate away from their maximum power point (MPP), a condition that requires an enhancement in PV module thermal behavior assessment. Consequently, there is a growing need for advanced thermal models that account for electrical operating conditions to ensure accurate temperature prediction under all operating scenarios. While traditional thermal models primarily depend on meteorological inputs, they typically neglect the Electrical Operating Status (EOS). Overlooking this issue can lead to significant prediction errors—up to 5–7 °C—especially during operation away from MPP. The proposed investigation developed an enhanced thermal model incorporating EOS dependency by including the ratio of measured current to the calculated current at MPP as an additional input. Two cases of the Faiman and Sandia models were optimized using Genetic Algorithm, Particle Swarm Optimization, non-linear least squares, and polynomial regression. Optimization is performed using three identical PV systems operating under reference EOS conditions: open circuit, short circuit, and MPP. Results demonstrate that EOS-integrated models significantly improve temperature prediction accuracy. The EOS sensitive models achieved prediction errors as low as 0.1–1.13 % and R^2 values above 0.91, outperforming traditional models that exhibited errors from 2 to 29 %. These findings support the need for EOS-aware thermal modelling in modern PV system design and operation.

1. Introduction

As the installed photovoltaic capacity is increasing rapidly, the issue of overgeneration—when electricity supply exceeds demand—is inevitable [1]. To maintain grid stability during these periods, system operators might need to curtail PV output generation by intentionally operating in points other than the maximum power point (MPP) [2]. This operational shift has implications for the thermal behavior of PV modules [3]. This deviation from standard operation requires thermal models to account for off-MPP operating conditions. Accurately modeling these scenarios is essential for assessing system performance and reliability assessments especially in high-penetration contexts where curtailment may become a regular practice [4–7]. PV cell temperature plays a key role in forecasting and estimation of the electrical performance of PV systems [8].

Traditionally, grid management has been based on the principle of matching power generation with immediate consumption or storage. Consequently, the idea of overbuilding PV capacity and intentionally curtailing excess generation has been seen as inefficient and wasteful. However, recent studies have confronted this typical sense [9–11] by strategically overbuilding PV systems and selectively limiting output during periods of high solar irradiation. As a result, it is increasingly

* Corresponding author. Department of Electric, Electronics and Computer Engineering, University of Catania, Viale Andrea Doria 6, Catania, 95125, Italy.
E-mail address: amrosama@eng.psu.edu.eg (A. Osama).

https://doi.org/10.1016/j.solmat.2025.113925
Received 13 June 2025; Received in revised form 6 August 2025; Accepted 26 August 2025

likely that grid-connected photovoltaic systems will operate at points different from the maximum power point in the near future. With the advancement of new installation solutions and technologies, a reliable standard operating procedure became essential, provided by international initiatives such as the International Energy Agency (IEA) and the Photovoltaic Power Systems Program (PVPS) Task 13 [43].

While the electrical efficiency of silicon-based PV modules has improved, reaching up to 23 % in commercial applications [12], still a significant portion of the received solar irradiance is converted into heat, increasing the cell temperature [13]. Most PV cell technologies have negative MPP thermal coefficients, which implies that the efficiency of a PV module degrades at an average rate of approximately 0.4 % for every 1 °C rise in cell temperature beyond the standard test condition (STC) [14].

Various thermal modelling approaches have been explored in the literature, each customized to different research objectives and accuracy requirements [15]. Dynamic thermal models, in particular, offer significant potential for estimating module temperature as they account for transient effects [16,17]. Dynamic thermal models have various approaches, including first-order differential equations, finite difference methods, and frequency-domain techniques [18]. However, these models are complex and require substantial computational resources, time, and effort [19]. Instead of treating the PV module as a single block of material and using one heat balance equation, dynamic thermal modeling separates each layer of the PV module. It considers each layer based on the thermal resistance concept, taking into account the physical and thermal properties of each layer.

Tuncela et al. [20] developed a transient thermal model to estimate PV module temperature, incorporating hourly meteorological data such as wind speed, wind direction, module parameters, and site-specific information. The model's performance was validated, achieving mean absolute error (MAE) and mean bias error (MBE) values of 2.61 °C and −1.64 °C, respectively, for daytime module temperature estimations. Korab et al. [21] proposed a dynamic thermal model based on the Finite Difference Method, optimized using the Particle Swarm algorithm. Experimental validation under rapidly changing atmospheric conditions showed that the temperature estimation error remained within 9 °C, leading to a PV power generation estimation error of less than 3.6 %.

Since the electrical characteristics of PV modules are temperature-dependent, integrating thermal effects into the modeling process helps improve the reliability of power output forecasts. However, capturing the interactions between electrical and thermal responses in PV modules introduces considerable modeling complexity. G. Tina [22] introduced an integrated electrical–thermal model that estimates the temperature distribution across various PV layers. His findings indicated that electrical parameters are highly sensitive to changes in cell temperature and local weather conditions. He also explored how different electrical operating points influence the current-voltage (IV) characteristics, revealing increased inaccuracies in thermal models under variable electrical conditions. Likewise, Gu et al. [23] validated a coupled electrical-thermal model for monofacial PV modules, emphasizing the importance of radiative and convective thermal resistances in determining thermal-electrical behavior, while noting that conductive resistance may be neglected in certain scenarios for simplicity. In addition, thermal resistance-based optical–electrical–thermal models have been applied to bifacial PV modules to simulate both daily and long-term performance [24]. Despite these developments, many existing models still fall short in precisely estimating cell temperatures and accurately replicating real-world electrical behaviors, often due to inefficient or incompatible coupling methods [25]. Achieving greater accuracy in electrical–thermal predictions calls for the integration of a more refined thermal model with a reliable and robust electrical modeling framework.

As a result, steady-state thermal models (SSTMs) are commonly employed to estimate module temperatures. To simplify calculations, the SSTMs typically disregard the thermal capacity of PV modules and transient effects [26]. Therefore, it is assumed that the climatic variables influencing PV module performance remain constant over short time intervals, where the steady-state thermal modeling can be applied efficiently [27]. The SSTMs are computationally efficient and relatively simple to implement. However, the assumptions used to develop such simple models lead to inaccuracies, resulting in either an overestimation or an underestimation of module temperatures. Over the years, numerous SSTMs have been developed to accommodate different installation configurations.

These SSTMs are based on simplified heat transfer equations with empirically determined parameters [28] or entirely empirical equations [29]. Some models also incorporate system-dependent properties, material characteristics, and parameters related to different assembly configurations. Traditional models, such as those developed by Faiman [28], Sandia [30], and Skoplaki [31] employ empirical correlations based on ambient temperature, solar irradiance, and wind speed to estimate the module temperature. These models' coefficients depend on the installation configurations and module technologies [32].

These models have been widely used in simulation software tools due to their simplicity and ease of implementation [33,34]. However, these empirical models often require specific coefficients that can vary based on mounting configurations and module types, leading to potential inaccuracies when applied universally. NOCT thermal model is one of the most well-known models for its simplicity [35]. It depends on the NOCT temperature specified by the PV module's manufacturer, as well as the ambient temperature and irradiance. Mattei et al. [59] proposed an energy balance-based thermal model to estimate module temperatures using three environmental variables. The validation with the experimental data revealed a root mean square error of 2.24 °C and a relative RMSE of 19.8 %.

Recent advancements have focused on enhancing the accuracy and reliability of these thermal models. One significant improvement involves integrating dynamic aspects into the traditionally static models to account for transient environmental conditions. For instance, Herteleer et al. [36] proposed methods to improve the accuracy of equation-based thermal models at second-to-minute timescales by incorporating dynamic responses to changing conditions. Additionally, the application of artificial intelligence (AI) and machine learning techniques has emerged as a promising approach to refining thermal predictions. Wang et al. [37] introduced a physics-informed machine learning model that efficiently estimates the convective cooling rates of PV arrays with various geometric configurations, thereby enhancing the precision of temperature predictions. These advancements contribute to more accurate performance assessments and optimized designs of PV systems, ultimately leading to increased energy efficiency and reliability.

When a PV system operates in a point other than the MPP, part of the electrical energy that wasn't absorbed by the module is converted to another form of energy, mostly thermal energy, elevating the module temperature [38]. The PV operation in Short circuit (SC) and open circuit (OC) status is one of the most serious faults that need to be detected and avoided [39]. A short circuit can be caused by many reasons, some of which are poor wiring, a damaged junction box, animal damage, water infiltration, and a faulty bypass diode [40]. It can happen between two points in the same string or between different strings. Open circuit condition, on the other hand, occurs when module terminals are disconnected, making the current of all the modules in the same string zero. Such faults are often caused by broken cells, damaged connections between them, loose connections, and defective power cables due to aging [41]. During the real operating condition, the PV module can operate at a voltage higher than one of the MPP or at a current higher than one of the MPP, causing a significant reduction in the module productivity. It is reported that such miss-perform can stimulate thermal stresses, especially the short circuit faults, which could lead in some conditions to fire hazards [42].

Many research investigated the available SSTMs and assessed the accuracy of the most commonly used ones in the literature [43,45,58].

These investigations reveal that SSTMs are generally not sensitive to the instantaneous operating point on the I-V characteristic curve. Many of these models were developed on the hypothesis of considering the photovoltaic module as non-producing electrical energy system extracted from the system [44]. Other models derived their coefficients from experimental measurements conducted under open-circuit conditions, which do not reflect real operational states.

Even thermal models based on energy balance principles that incorporate electrical efficiency often rely on coefficients developed for low-efficiency PV modules. Furthermore, these models typically use the electrical efficiency under the STC rather than accounting for the actual, dynamic electrical operating status. This simplification tends to assume a higher thermal conversion rate, potentially leading to overestimations of module temperature for modern high-efficiency PV modules (efficiency >20 %).

Moreover, as demonstrated in Ref. [45] the electrical operating condition significantly influences the thermal behaviour of PV modules and should therefore be considered in thermal modeling. With the global trend toward overbuilding grid-connected PV capacity, scenarios requiring electrical output regulation are becoming more common, directly impacting thermal performance. Thus, developing a thermal model that incorporates the actual electrical operating conditions will enhance monitoring capabilities under non-MPP conditions, which is the primary objective of the present study.

Therefore, the thermal modeling of PV module temperature (T_m), with a focus on sensitivity to the system's electrical operating status, is investigated. Modifications are proposed to two of the most commonly used thermal models in the literature and simulation software—namely, the Faiman model and the Sandia model—by incorporating the ratio between the instantaneous current and the current at MPP under the given environmental conditions. This ratio serves as a representative indicator of the Electrical Operating Status.

To enhance the practical applicability of the models, the thermal coefficients are optimized across a range of electrical operating conditions, including OC, SC, and MPP scenarios. Both the Faiman and Sandia models are optimized in various forms using metaheuristic and stochastic optimization algorithms, specifically Genetic Algorithm and Particle Swarm Optimization, in addition to non-linear least squares regression analysis.

The current investigation is structured as follows: Section 2 presents the modifications to the thermal models, including the integration of electrical operating condition sensitivity and coefficient optimization; Section 3 describes the experimental setup and measurement procedures; Section 4 analyzes the performance of the optimized thermal models, comparing their accuracy to measured data and existing models from the literature; and Section 5 concludes the study by identifying the optimal thermal model that achieves the highest level of accuracy.

2. PV thermal models analysis

The prediction of the cell temperature of the PV module that operates at specific environmental conditions is crucial to estimate the electrical production of such a system and for monitoring the overall performance to spot any unexpected faults. The Faiman thermal model [46] presented in Eq. (1) is one of the most used models in the literature and recommended by the IEC 61853-2 standard [47,48] for its simplicity and its potential to optimize its coefficients to adapt to the emerging installation solutions. Additionally, the Faiman model is utilized in PVsyst simulation software tool for thermal modelling [49,86]. The Faiman model is based on the assumptions of a negligible effect of the thermal mass of a conventional (i.e., glass front, plastic back) PV panel on its heat exchange with the surroundings.

$$T_m = T_a + \frac{\alpha G_{POA}\,(1-\eta_e)}{U_0 + U_1 \omega_s} \tag{1}$$

Where:

T_a: Ambient temperature, [°C].

G_{POA}: Plane of array irradiance, [W/m^2].

ω_s: The measured wind speed (2 m above the ground or around 0.5 m above the module), [m/s]

U_0: Heat transfer coefficient expressing the effect of the radiation on the module temperature, [W/m^2°C].

U_1: Heat transfer coefficient expressing the cooling by the wind, [Ws/m^3°C].

α: The absorption coefficient of the front glass of the PV module is 0.9 [50].

η_e: The electrical efficiency of the module at standard test conditions, [%].

The Faiman model was investigated for monofacial PV modules with mono-crystalline (c-Si) and poly-crystalline (pc-Si) cell technology, which shows a similarity between the developed thermal coefficient for the examined PV panels installed in the same configuration. It has been calculated that for the monofacial PV modules mounted on an open rack, the U_0 and U_1 coefficients are equal on average ($U_0 = 25$ W/m^2°C, $U_1 = 1.2$ W/m^3°C) [51]. It is worth mentioning that several works have been established based on the formula of the Faiman model, adopting the thermal coefficients for different installation configurations [52,53], better accuracy prediction [31], or to include the dynamic response in such a steady-state thermal model [21].

Sanida thermal model can also be called the king model. [54], showed a great potential through the exponential form, see Eq. (2) [55]. Sandia National Laboratories developed it based on an energy balance while using the instant weather variable as an input for the module temperature prediction [29,54].

$$T_m = T_a + G_{POA} \cdot e^{a+b\cdot\omega_s} \tag{2}$$

Where both (a) and (b) are empirical coefficients whose values are determined according to the PV module technologies and installation configuration. It has been stated that for a monofacial (Glass/cell/polymer sheet) installed in an open rack mounting, the empirical coefficients (a) and (b) have the values of −3.56 and −0.075, respectively [43]. Moreover, it is worth mentioning that there is no indication in the literature about the electrical operating conditions of the examined PV system for the extraction of the empirical coefficients. Yet, Keddouda et al. [56] recently recalibrated the formula calibration for higher accuracy, especially for the MPP operating systems. Both the System Advisor Model (SAM) software, developed by NREL, and the Python-based PVlib software are simulation software tools that utilize the Sandia thermal model for the performance modelling of PV systems [86].

2.1. Thermal models integrated with electrical operating condition sensitivity

While most thermal models treat the PV module as a flat plate from a thermal balance perspective [57], neglecting the impact of the electrical energy extracted from the system (e.g., the Sandia (Eq. (2)) and NOCT models). A few models in the literature account for the electrical efficiency of the PV module (η_e) [44], (e.g.: Faiman model (Eq. (1)), Servant [58], and Mattei [59]) which are expected to enhance prediction accuracy. The limitations of such models are the following:

- The electrical efficiency is considered to be sensitive only to the cell temperature while neglecting the actual electricity extracted from the PV module [60].
- The efficiency considered in some models is assumed constant and equal to the STC one at MPP conditions.

- The electrical efficiency is not a true representation of the electrical operating condition of the PV system, which can be misleading.

The thermal behavior of a PV module has been confirmed to be influenced by the electrical operating condition of the system. This has been proved experimentally by a study [45] where the temperatures of PV modules operate at reference electrical conditions; SC status (zero voltage and maximum current), MPP (optimal voltage and current for the environmental operating condition), and OC condition (maximum voltage and zero current) have been analyzed. Fig. 1 shows an experimental measurement of the electrical and thermal performance for the three PV systems simultaneously.

Under real operating conditions like the OC and the SC modes—-where no electrical power is extracted and thus $\eta_e = 0$—such models are expected to predict the same module temperature. Yet, experimental measurements (Fig. 1 [45]) contradict this assumption, showing noticeable temperature differences under OC and SC conditions. This highlights the need for improved thermal models that explicitly incorporate the influence of electrical operating conditions on PV module temperature.

An energetic analysis of the behavior of PV cells, particularly focusing on joule losses that are thermal energy sources, can provide deeper insights into the influence of electrical operating conditions on the thermal response of PV modules. As illustrated in Fig. 2, while solar irradiance is transmitted through the glass layer and absorbed by the PV cell, a significant portion of the absorbed solar spectrum—mainly in the infrared (50–55 %) and ultraviolet (<4 %) wavelengths—is converted into heat. This process elevates the module temperature based on heat exchange with the surrounding environment [61]. In contrast, only a portion of the visible light spectrum contributes to the generation of photocurrent by releasing electrons under specific environmental and operating conditions.

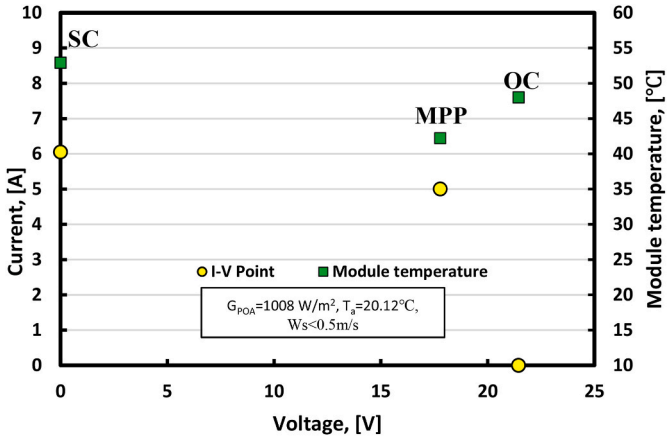

Fig. 1. The PV module temperature at reference electrical operating points given the environmental operating conditions.

Considering the one-diode equivalent circuit model, the absorbed solar energy is converted into useful electrical power (P_{out}) delivered to the load and dissipated internally as thermal losses (P_{th}). The lumped contributors to thermal dissipation include the diode, series resistance (R_s), and shunt resistance (R_{sh}). The extracted electrical output power, P_{out}, as defined in Eq. (3), represents the useable energy drawn from the system. On the other hand, P_{th}, see Eq. (4), encompasses the internal losses within the PV module, primarily due to Joule heating [62,63]. The shunt resistance (R_{sh}) represents leakage currents across the junction or through defects [64], while the series resistance (R_s) is influenced by the output current (I) [65], as shown in Eq. (5). Additionally, the power dissipated in the diode arises mainly from carrier recombination and other non-ideal effects in the p-n junction, as described in Eqs. (5, 6 and 7) [66] considering the dynamic nature of the diode resistance [67].

Each component of the thermal losses defined in Eq. (7) is explicitly dependent on one of the internal currents (I, I_{sh}, or I_d) in the one-diode model [90]. These currents are interdependent and are functions of solar irradiance, cell temperature, and the operating point (voltage and current) of the PV module, as governed by the complete set of equations for the one-diode model.

The electrical load power, P_{out}, is determined by the current (I) and voltage (V) at a specific point on the module's I–V curve, which, in turn, defines the internal operating conditions, including the diode and shunt currents (I_d, I_{sh}). When the module operates near the MPP, P_{out} is maximized. For a given level of photogenerated power, a higher P_{out} indicates reduced internal heat dissipation, thereby minimizing P_{th}.

In contrast, under open-circuit conditions (P_{out}=0), no electrical power is extracted, and all the photogenerated current—after accounting for I_{sh} and I_d—is dissipated internally, predominantly in the diode and shunt resistance paths. Due to the typically high value of the R_{sh}, the resulting current dissipation is relatively low. Under short-circuit conditions, although no module output voltage is present, the current is maximized. Consequently, most of the generated power is dissipated internally, particularly through the series resistance, due to its relatively lower value compared to the shunt resistance. This results in higher Joule losses in R_s, leading to greater thermal load than in the open-circuit condition under the same ambient temperature, plane-of-array irradiance, and wind conditions.

$$P_{converted} \approx P_{th} + P_{out} \tag{3}$$

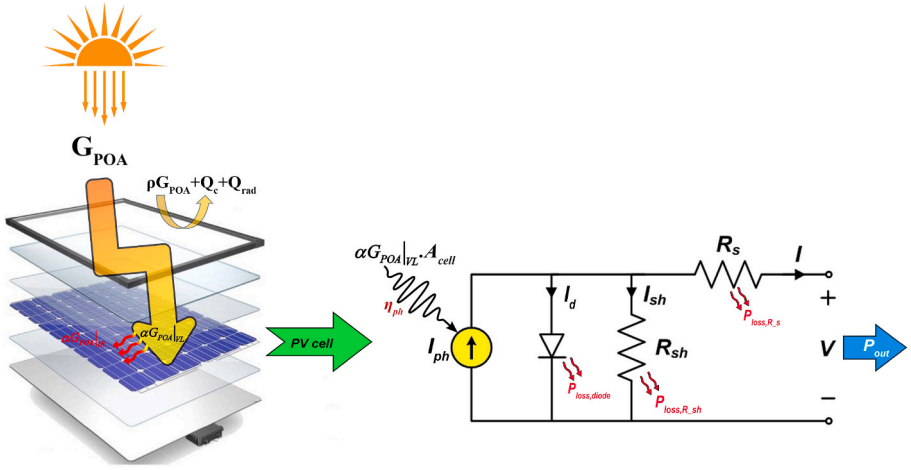

Fig. 2. Schematic of the power balance of the PV module considering the single diode model equivalent circuit model.

$$P_{th} = P_{loss,R_s} + P_{loss,R_{sh}} + P_{loss,diode} \tag{4}$$

$$P_{th} = I^2 R_s + I_{sh}^2 R_{sh} + \underline{I_d^2 r_d} \tag{5}$$

$$r_d \approx \frac{V_T}{I_d} \tag{6}$$

$$P_{th} = I^2 R_s + I_{sh}^2 R_{sh} + I_d V_T \tag{7}$$

Accordingly, from the perspective of the single-diode equivalent circuit model, current is a key variable influencing the thermal behavior of the PV cell, particularly with regard to thermal losses. The various types of thermal losses presented in Eq. (7), which are linked to the electrical behavior of the PV cell, are directly dependent on the current value. Moreover, current is less sensitive to variations in cell temperature, reducing the risk of misinterpretation. According to the IEC 61853-1 standard [68], the temperature coefficient of current for silicon-based photovoltaic modules typically ranges from approximately 0.04 %–0.06 %/°C, which is relatively small. In contrast, voltage exhibits a much higher sensitivity to cell temperature, with a typical temperature coefficient around −0.30 %/°C [69]. Therefore, current can be regarded as having a relatively stable behavior with respect to temperature variations. As a result, in the absence of soiling or shading, the measured current serves as a reliable indicator of the instantaneous plane-of-array irradiance incident on the module, without being significantly affected by cell temperature fluctuations.

The electrical operating status (EOS) describes the position of the PV module's operating point on the I–V characteristic curve, which is determined by the instantaneous meteorological conditions and the PV cell temperature. Each point on the I–V curve corresponds to a specific current and voltage under given operating conditions. Operating at the MPP requires the module to function at both the maximum power current (I_{mpp}) and maximum power voltage (V_{mpp}) under those specific conditions [70]. Since voltage is highly sensitive to cell temperature, the maximum power current can be approximately modeled as a function of irradiance alone [71].

To represent EOS using a dimensionless parameter, it must consistently have a positive value and provide a stable and accurate indication of the operating point's location on the I–V curve. The current at the MPP can serve as a reliable reference for this purpose. Therefore, EOS can be quantified using the current ratio, defined as the ratio of the instantaneous measured current (I) to the expected MPP current (I_{mpp}) under the same irradiance and ambient temperature conditions, as shown in Eq. (8). The value of I_{mpp} can, in turn, be estimated relative to the STC, as described in Eq. (9) [72]. Accordingly, under open-circuit conditions, the EOS equals 0; under short-circuit conditions, the EOS is greater than 1; and for ideal MPP operation under STC, the EOS is approximately equal to 1.

$$EOS = \frac{I}{I_{MPP}} \tag{8}$$

$$I_{MPP} \simeq \frac{G_{POA}}{G_{POA,STC}} \times I_{MPP,STC} \tag{9}$$

Where:

$G_{POA,STC}$: The plane of array irradiance at STC, $G_{POA,STC} = 1000\ \mathrm{W/m^2}$

$I_{MPP,STC}$: The current of the PV module operates at maximum power point at STC, which is mentioned in the module's datasheet, [A].

Fig. 1 shows that the module temperature exhibits a quadratic trend with respect to the EOS of the PV module. Therefore, it is essential to develop thermal models that incorporate the EOS as an input variable to improve prediction accuracy. This behavior can be mathematically represented by a quadratic equation, as shown in Eq. (10), where c, d, and e are constant coefficients.

While the quadratic term presents the joule losses, the linear term serves as a complementary component that accounts for possible temperature-reducing effects associated with current, such as the extracted P_{out}. Essentially, this linear term causes the curve to bend downward, as illustrated in Fig. 1, highlighting that the relationship between current and temperature rise is not purely quadratic. Additionally, the constant term acts as an empirical calibration offset introduced during curve fitting. It accounts for thermal capacitance effects and compensates for variations in environmental conditions to prevent overestimation—especially under open-circuit conditions, where no current is flowing.

$$\text{Thermal modeling sensitivity to the EOS} = c \cdot X^2 + d \cdot X^1 + e \cdot X^0 = c\left(\frac{I}{I_{MPP}}\right)^2 + d\left(\frac{I}{I_{MPP}}\right)^1 + e\left(\frac{I}{I_{MPP}}\right)^0 \tag{10}$$

While the thermal losses associated with the EOS are primarily influenced by the received irradiance—and consequently by the current—integrating the EOS into both the Sandia and Faiman thermal models is formulated through a quadratic expression related to the plane-of-array irradiance. This formulation can adopt various mathematical forms, each potentially affecting the model's behavior differently. To explore this, two distinct cases (Case 1 and Case 2) are proposed, each incorporating the EOS as a quadratic input into the thermal models. Case 2 additionally includes electrical efficiency as an input. In contrast, Case 0 represents the baseline scenario, where the standard thermal models are recalibrated using the existing dataset, as summarized in Table 1.

2.2. Regression and optimization algorithms analysis

Extracting the optimal values of the empirical coefficients for each form of the physical thermal model requires the use of optimization algorithms capable of minimizing error levels. Since each algorithm employs its own iterative approach to optimization, three regression and optimization algorithms will be analyzed in this study.

Table 1
Modified thermal models cases integrated with the electrical operating status.

Thermal model	Developed thermal model	Eq. No.	Empirical coefficient
Modified Sandia model integrated with the electrical operating status			
Sandia-Case 0	$T_m = T_a + G_{POA} e^{a+b\omega_s}$	2	a,b
Sandia-Case 1	$T_m = T_a + G_{POA} e^{a+b\omega_s}\left(c\left(\frac{I}{I_{MPP}}\right)^2 + d\left(\frac{I}{I_{MPP}}\right) + e\right)$	11	a,b,c,d,e
Sandia-Case 2	$T_m = T_a + G_{POA} e^{a+b\omega_s}\left(c\left(\frac{I}{I_{MPP}}\right)^2 + d\left(\frac{I}{I_{MPP}}\right) + e - \eta_e\right)$	12	a,b,c,d,e
Modified Faiman model integrated with the electrical operating status			
Faiman-Case 0	$T_m = T_a + \frac{\alpha G_{POA}}{U_0 + U_1\omega_s}$	13	U_0, U_1
Faiman-Case 1	$T_m = T_a + \frac{\alpha G_{POA}\left(c\left(\frac{I}{I_{MPP}}\right)^2 + d\left(\frac{I}{I_{MPP}}\right) + e\right)}{U_0 + U_1\omega_s}$	14	U_0, U_1,c,d,e
Faiman-Case 2	$T_m = T_a + \frac{\alpha G_{POA}\left(c\left(\frac{I}{I_{MPP}}\right)^2 + d\left(\frac{I}{I_{MPP}}\right) + e - \eta_e\right)}{U_0 + U_1\omega_s}$	15	U_0, U_1,c,d,e

- **Genetic algorithm (GA)**

Genetic Algorithms are evolutionary optimization techniques inspired by natural selection and genetics [73]. They operate through iterative cycles of selection, crossover, and mutation. Initially, a population of candidate solutions (chromosomes) is randomly generated [74]. Each chromosome represents a potential set of coefficients for the thermal model. The fitness of each candidate is evaluated using an objective function, such as the root mean square error (RMSE) between predicted and experimental thermal outputs [75]. High-fitness candidates are selected probabilistically to reproduce. During crossover, pairs of chromosomes exchange genetic information to create offspring, while mutation introduces small random changes to maintain diversity [76]. This process repeats until convergence criteria (e.g., maximum iterations or minimal fitness improvement) are met. The GA has the advantage of being robust in escaping local minima due to stochastic operations [77]. Moreover, it's suitable for non-convex, discontinuous, or multi-modal objective functions, and there are no requirements for gradient information.

- **Particle swarm optimization (PSO)**

Particle Swarm Optimization is a heuristic optimization method inspired by the collective behavior of swarms, such as birds flocking or fish schooling [78]. A swarm of particles (candidate solutions) navigates the search space, adjusting their positions based on individual and group experiences. Each particle tracks its personal best position (p_{best}) and the global best position (g_{best}) of the swarm iteratively [79]. The velocity and position updates follow [80]:

$$\nu_i^{t+1} = \omega \cdot \nu_i^t + c_1 r_1 \left(P_{best,i} - x_i^t\right) + c_2 r_2 \left(g_{best,i} - x_i^t\right) \tag{16}$$

$$x_i^{t+1} = x_i^t + \nu_i^{t+1} \tag{17}$$

where ω is inertia weight, c_1,c_2 are cognitive/social coefficients, and r_1, r_2 are random numbers in [0,1]. The PSO has an efficient exploration-exploitation balance through social collaboration [81]. In addition, it has low computational complexity and is parallelizable. Moreover, it is effective for continuous, high-dimensional spaces.

- **Non-linear least squares (NLLS)**

Non-Linear Least Squares is a regression technique used to fit a model to data when the relationship between variables is non-linear [82]. Unlike linear least squares, which assumes a straight-line relationship, NLLS iteratively refines parameter estimates using methods such as the Gauss-Newton or Levenberg-Marquardt algorithms [83]. The advantage of NLLS is its ability to model complex relationships and provide accurate parameter estimates for non-linear systems, making it valuable in scientific and engineering applications. For PV thermal models, the objective is to find coefficients x that minimize the sum of squared residuals between model predictions and data:

$$Minimize\, f(x) = \sum_{i=1}^{N} \left(T_{m,i} - T_{model,i(x)}\right)^2 \tag{18}$$

The Levenberg-Marquardt algorithm is commonly used, which hybridizes gradient descent and Gauss-Newton methods. The update rule is:

$$x^{k+1} = x^k - \left(J^T J + \lambda I\right)^{-1} J^T r \tag{19}$$

where **J** is the Jacobian matrix, **r** is the residual vector, and λ is a damping parameter.

- **Polynomial Regression**

Polynomial regression extends linear regression by fitting a nonlinear relationship between independent variables (e.g., irradiance, ambient temperature, and wind speed) and the dependent variable (PV module temperature) using polynomial terms. This method is useful for modeling curved trends in data while preserving the interpretability and computational efficiency of linear regression. The model remains linear in its coefficients, as shown in Eq. (17), where the coefficients are estimated to minimize the error.

$$y = \beta_0 + \beta_1 x_1 + \beta_2 x_2 + \ldots\ldots + \beta_n x_n \tag{20}$$

Polynomial linear regression has the advantage of capturing nonlinear relationships between variables. In addition to its simple implementation, it is also extensible to multiple variables and higher-degree terms.

To evaluate the precision of the optimized coefficients for the models mentioned in Table 1 against the experimental measurements, statistical metrics are introduced [84]. The Mean Squared Error (MSE), Mean absolute error (MAE), Mean Absolute Percentage Error (MAPE), Root Mean Square error (RMSE), and the coefficient of determination (R^2) are utilized for error estimation, as can be expressed in the following formulas [60,85,88], (see Eq 21, 22, 23, 24 and 25).

$$MSE = \frac{1}{n}\sum_{i=1}^{n}\left(T_{m,i} - T_{c,i}\right)^2 \tag{21}$$

$$MAE = \frac{1}{n}\sum_{i=1}^{n}\left|T_{m,i} - T_{c,i}\right| \tag{22}$$

$$MAPE = \frac{1}{n}\sum_{i=1}^{n}\left|\frac{T_{m,i} - T_{c,i}}{T_{m,i}}\right| \times 100 \tag{23}$$

$$RMSE = \sqrt{\frac{1}{n}\sum_{i=1}^{n}\left(T_{m,i} - T_{c,i}\right)^2} \tag{24}$$

$$R^2 = 1 - \frac{\sum_{i=1}^{n}\left(T_{m,i} - T_{c,i}\right)^2}{\sum_{i=1}^{n}\left(T_{m,i} - \overline{T_m}\right)^2} \tag{25}$$

where $T_{m,i}$ and $T_{c,i}$ are the measured and calculated temperatures, respectively, and $\overline{T_m}$ is the mean of the measured temperature, while n is the number of samples.

3. Experimental test setup and measurement devices

An experimental setup consists of three photovoltaic (PV) sets installed on the campus of Jaén University in Spain. The installation is located on the roof of the Faculty of Engineering building at coordinates 37°47′14.0″N, 3°46′40.5″W. Each PV set comprises two identical PV modules, each rated at 100 W, connected in parallel. The specifications of the modules are provided in Table 2.

Each PV set is designed to operate at a specific electrical condition:

- **PV Set 1** operates under short-circuit conditions,
- **PV Set 2** operates under open-circuit conditions
- **PV Set 3** operates at the maximum power point, using an electronic load.

The PV sets are mounted 1.5 m above the roof surface as free-standing rooftop installations, oriented towards the south (see Fig. 3).

The electrical performance of the three PV sets—specifically, the short-circuit current of Set 1 (I-Set 1 = I_{sc}), the open-circuit voltage of Set 2 (V-Set 2 = V_{oc}), and the maximum power current and voltage of Set 3 (I-Set 3 = I_{MPP}, V-Set 3 = V_{MPP})—has been measured and recorded for further analysis. An electronic load (EL9000B) is used to track the MPP

Table 2
Specification of the PV module.

Specification	Value
Model name	WS-100/12V
Panel brand	WAAREE
Material	Polycrystalline
Dimensions in mm	1150 × 675 × 35
Short-circuit current ($I_{sc,STC}$), [A]	6.07
Open circuit voltage ($V_{oc\ STC}$), [V]	21.97
Maximum power ($P_{MPP,\ STC}$), [W]	100
Maximum power voltage ($V_{MPP\ STC}$), [V]	17.47
Maximum power current [($I_{MPP,\ STC}$), [A]	5.73
Open circuit voltage temperature coefficient, [%/°C]	−0.2941
Short circuit current temperature coefficient, [%/°C]	0.0681
Maximum power temperature coefficient, [%/°C]	−0.3845
Nominal Operating Cell Temperature, [°C]	46
Module efficiency at standard test conditions (η_{STC}), [%]	12.88

Fig. 3. Photograph of the experimental apparatus at University of Jaén (Spain).

of PV Set 3 under varying ambient conditions. This electronic load features a built-in maximum power point tracking (MPPT) algorithm capable of identifying the global MPP, and it is software-controlled.

The real-time values of maximum power voltage and current are used directly for monitoring and analysis through a LabVIEW-based application (see Fig. 4 [45]). The thermal behavior of the three PV sets, expressed through the module temperature, is monitored using PT100 sensors.

Meteorological variables, including the plane of array irradiance (G_{POA}) and ambient temperature (T_a), are measured using a DATASOL MET calibrated reference cell, which is mounted above the modules and aligned parallel to their surface (see Fig. 3). Wind speed (ω_s) is measured using an anemometer installed on the experimental setup. Details of the experimental setup, measurement devices, and their respective accuracies are provided in Ref. [45].

4. Results and discussion

Measurements were conducted from March 2024 and continued for four months, with data recorded at 30-s intervals. For improved stability, the data were averaged to 5-min intervals. Throughout the monitoring period, periodic checks were performed on the three PV sets—each operating under different electrical status—to ensure the reliability of both the system and the recorded data.

4.1. Experimental measurements sample

On a clear-sky day, taken as a representative example from the monitoring period, the influence of electrical operating status on the thermal behavior of the PV modules is clearly observable, as illustrated in Fig. 5. On March 11th, the daily average plane-of-array irradiance and ambient temperature were 770 W/m^2 and 18.12 °C, respectively. Under these conditions, the module in PV Set 3, operating at MPP, recorded a daily average temperature of 35.54 °C and reached a maximum of 46.44 °C at 1:55 p.m., when the G_{POA} peaked at 1012 W/m^2. The daily average temperature has been calculated during daytime with G_{POA}>200W/m^2.

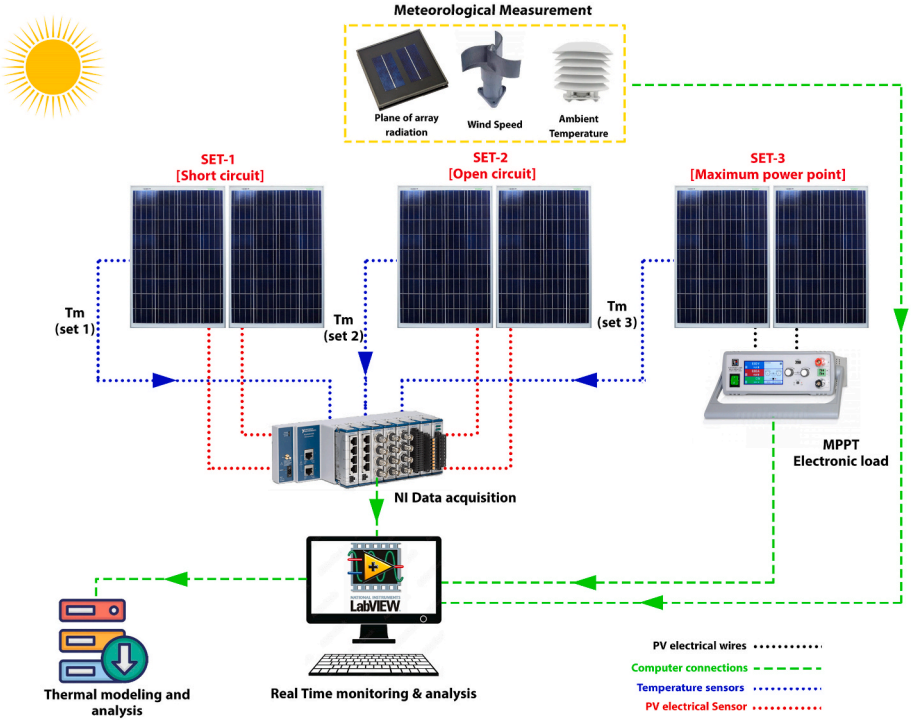

Fig. 4. Methodology of the experimental setup and analysis [45].

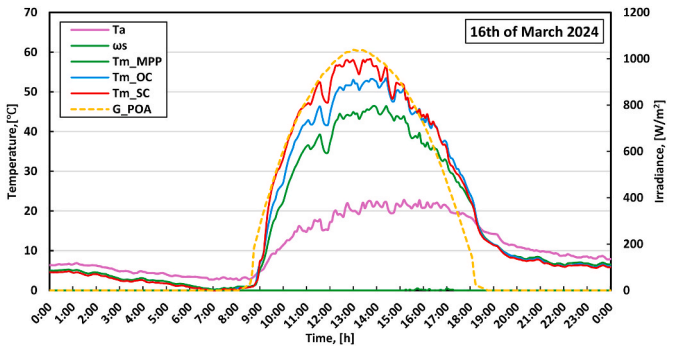

Fig. 5. Sample of daily measured meteorological variables, and PV module temperatures at the examined extreme electrical operating conditions.

In contrast, the short-circuited module in PV Set 1 exhibited a higher daily average temperature of 44.58 °C—approximately 25.42 % higher than that of the MPP module—with a maximum temperature difference of 11.78 °C. Meanwhile, the open-circuited module in PV Set 2 had an average temperature of 41.45 °C and a maximum of 53.37 °C, which is 16.62 % higher than the MPP module's average, with a maximum temperature difference of 6.93 °C.

Moreover, to present the electrical performance, the measured current and EOS are shown in Fig. 6. As expected, the open-circuited PV Set 2 produces no current (I-OC = 0). In contrast, the measured DC currents for both the MPP-operating Set 3 (I-MPP) and the short-circuited PV Set 1 (I-SC) follow a parabolic pattern, corresponding closely to the irradiance intensity throughout the day.

Additionally, the EOS exhibits some discrepancies at low irradiance levels during early morning and near sunset. However, it remains stable for the rest of the day when irradiance exceeds 200 W/m^2—approximately 0.94 to 1.00 under MPP conditions and 1.06 to 1.08 under short-circuit conditions.

4.2. Thermal models optimization

The modified thermal model, which integrates the sensitivity to the EOS, has been introduced in several mathematical forms, as can be seen in Table 1 for both the Sandia and Faiman thermal models. Optimizing the coefficients of various thermal models is based on measured environmental and operational data of three PV sets operating at reference operating statuses (Open circuit, short circuit, and maximum power point). The measurements of four months have been considered in the analysis. Moreover, to ensure more reliable and stable data records, a filtration process was applied by excluding data points with irradiance levels below 150 W/m^2 and wind gusts exceeding 7 m/s. Following this, 70 % of the filtered dataset was used to train the optimization algorithms, while the remaining 30 % was reserved for evaluation and error

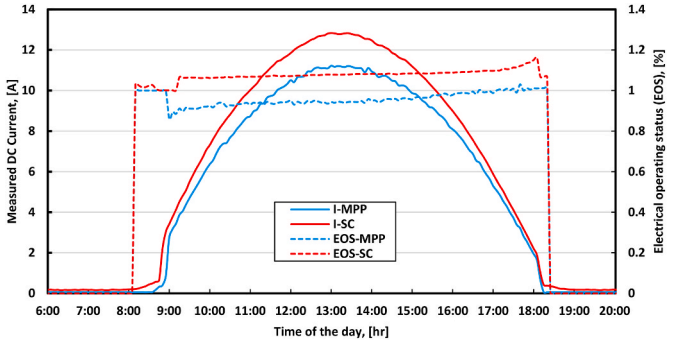

Fig. 6. Measured current and EOS of the examined systems on the 16th of March 2024.

analysis. To mitigate the risk of overfitting, both regularization and 5-fold cross-validation techniques were employed during the coefficient optimization process. All computations were carried out on a laptop equipped with an Intel Core Ultra 7 165H processor (3.80 GHz) and 32 GB of RAM, which enabled efficient execution of the optimization tasks.

The optimization of Case 0 was conducted using the full dataset, which includes measurements from all three EOS, to determine the coefficients a and b for the Sandia model and U_0 and U_1 for the Faiman model. In contrast, the optimization processes for Cases 1 and 2 were carried out in two stages. In the first stage, the primary coefficients of the Faiman (U_0, U_1) and Sandia (a, b) models were tuned using a dataset that includes only a subset of open-circuit measurements. The open-circuit condition ($\eta_e = 0$ and $I/I_{mpp} = 0$) was treated as the reference scenario, in which the integrated input EOS equals zero. In the second stage, the optimization focused on the additional coefficients introduced by the newly integrated quadratic EOS equation. This stage used the whole dataset encompassing all three EOS conditions— OC, MPP, and SC—while retaining the tuned coefficients from the first stage.

Three different optimization techniques were applied to each thermal model to determine accurate and trustworthy empirical coefficients. Among these, the GA was used to fine-tune the parameters of several thermal models, using real-world environmental and operational data. The GA was set up in MATLAB through the built-in function, with its main settings carefully chosen to encourage reliable convergence and thorough exploration of possible solutions. A population size of 100 individuals per generation was used, and the algorithm was allowed to run for up to 800 generations for less computation time, with the accuracy of the results by minimizing the sum of squared errors. Default values were used for other GA settings, including stochastic uniform selection, Gaussian mutation, and a crossover fraction of 0.8.

In addition to the GA, the PSO was also employed in this study to determine the optimal parameters by minimizing the RMSE between predicted and experimentally measured module temperatures. The PSO algorithm was configured with a swarm size of 100 particles and a maximum of 800 iterations. These settings were selected to ensure adequate convergence while effectively exploring the complex, multi-dimensional search space. The optimization was set to terminate automatically when the change in the objective function dropped below a threshold of 10^{-5}, balancing accuracy with computational efficiency.

Moreover, the NLLS was implemented using the Levenberg–Marquardt algorithm, which is well-suited for problems involving unbounded variables. An initial guess of zero was assigned to all model coefficients. The maximum number of function evaluations was set to 5000, and strict convergence criteria were enforced by specifying tolerance values of 10^{-10} for both the function value and step size. This setup aimed to enhance the accuracy and reliability of parameter estimation across all six thermal models. Furthermore, polynomial regression was applied by assuming a linear relationship with the dependent variable and a parabolic relationship with the EOS, in order to preserve the characteristic parabolic behavior of the thermal response with respect to the EOS.

The developed coefficients of the examined cases according to the aforementioned optimization parameters are presented in Table 3. It can be seen that both the GA and PSO algorithms have resulted in similar coefficients for each model's case investigated, despite the difference in the optimization methodologies. Moreover, for each model's case examined, the NLLS optimized coefficients are also similar to the ones developed by the GA and the PSO algorithms. For the Sandia Model, while the values of coefficients a and b are −3.56 and −0.075 in the literature, their values in the modified cases vary between −3.512 and −3.515 and −0.10604 to −0.1127, depending on the case selected, see Table 3. Moreover, the values of U_0 and U_1 in the newly modified Faiman models vary between 30.08 and 30. 166 and 3.659 to 3.905, depending on the chosen case of the modified version of the Faiman model, while the literature expresses their values of about 25 and 1.2, respectively.

Table 3
The empirical coefficients of the modified thermal models that include the electrical operating condition status.

Thermal model	Optimization algorithm	Empirical coefficient				
		a	b	c	d	e
Sandia	literature	−3.56	−0.075			
Sandia- Case 0	NLLS	−3.51509	−0.10604			
Sandia- Case 1	GA	−3.51200	−0.11270	3.07605	−3.09746	1.00113
	PSO	−3.51200	−0.11270	3.07762	−3.09911	1.00120
	NLLS	−3.51200	−0.11270	3.07756	−3.09905	1.00119
Sandia- Case 2	GA	−3.51200	−0.11270	0.76585	−0.64932	1.00118
	PSO	−3.51200	−0.11270	0.76961	−0.65315	1.00119
	NLLS	−3.51200	−0.11270	0.76962	−0.65315	1.00119
		U_0	U_1	c	d	e
Faiman	literature	25	1.2	–	–	–
Faiman- Case 0	NLLS	30.16600	3.65914	–	–	–
Faiman- Case 1	GA	30.08000	3.90500	3.07531	−3.09668	1.00162
	PSO	30.08000	3.90500	3.07868	−3.10008	1.00165
	NLLS	30.08000	3.90500	3.07869	−3.10010	1.00165
Faiman- Case 2	GA	30.08000	3.90500	0.77791	−0.66158	1.00180
	PSO	30.08000	3.90500	0.77075	−0.65421	1.00165
	NLLS	30.08000	3.90500	0.77080	−0.65426	1.00165
Polynomial Regression	$T_m = 0.981T_a - 1.3684\omega_s + 0.12G_{POA}\left(2.966\left(\frac{I}{I_{MPP}}\right)^2 - 3.108\left(\frac{I}{I_{MPP}}\right) + 0.241425 + \eta_e\right)$ Eq. (26)					

To gain deeper insight into the performance of the examined thermal models and their optimized coefficients, a statistical analysis was conducted using error metrics to evaluate the models under three extreme EOS, as summarized in Table 4. It can be noticed that integrating EOS sensitivity into the thermal models—both the modified Sandia and Faiman models for cases 1 and 2—significantly improves prediction accuracy by reducing overall prediction error compared to the typical model of case 0 for both Sandia and Faiman thermal models, despite the coefficients calibration.

Among the tested configurations, the modified Sandia models consistently demonstrated higher prediction accuracy compared to the modified Faiman models under the same conditions. Furthermore, regardless of the optimization algorithm used, Case 1 of the modified Sandia and Faiman models achieved the best accuracy across all scenarios.

Specifically, the modified Sandia model Case 1, optimized using the NLLS algorithm, achieved the highest overall accuracy with an R^2 of 0.927 and RMSE of 3.248 °C. This marks a notable improvement over the typical Sandia model using standard empirical coefficients, which yielded $R^2 = 0.897$ and RMSE = 3.876 °C. Similarly, other cases of the modified Sandia model also showed improved performance. Integrating the electrical efficiency and the EOS as in Case 2, optimized using NLLS, the model achieved $R^2 = 0.927$ and RMSE = 3.258 °C, confirming that both cases outperformed the standard Sandia model.

For Case 1 of the modified Faiman model, optimized with NLLS, also showed significant improvement, ranking seventh among all tested configurations with $R^2 = 0.927$, RMSE = 3.259 °C, and MSE = 10.621°C^2. Additionally, Case 2 of the modified Faiman model optimized with NLLS demonstrated improved accuracy with $R^2 = 0.9266$, RMSE = 3.2699 °C, MSE = 10.692°C^2, see Table 4. In contrast, the typical Faiman model without EOS sensitivity performed considerably worse, with $R^2 = 0.731$, RMSE = 6.268 °C, and MSE = 39. 296°C^2, reinforcing the effectiveness of incorporating the EOS in enhancing the predictive accuracy of thermal models. Also, the polynomial regression led to a simple equation, see Table 3, that is able to simply anticipate the module temperature with the sensitivity to the EOS, which has a relatively high accuracy with an average error metrics of $R^2 = 0.9226$, RMSE = 3.356 °C, and MSE = 11.268°C^2 as can be spotted in Table 4.

4.3. Thermal models evaluation at MPP operation

To ensure a more realistic evaluation, especially for predicting module temperature during the day, we assessed each model's response across various EOS examined. Fig. 7 illustrates this for module

Table 4
Error metrics of the overall prediction performance of the modified thermal models.

Thermal model	Optimization algorithm	Error metrics					Ranking Position
		MSE °C^2	RMSE °C	MAE °C	MAPE %	R^2	
Sandia	literature	15.02804	3.876602	3.155247	10.98624	0.897163	14
Sandia case 0	NLLS	15.50188	3.937243	3.178804	11.13453	0.893652	15
Sandia case 1	GA	10.54961	3.248016	2.71502	10.00341	0.927626	3
	PSO	10.5496	3.248015	2.715039	10.00353	0.927626	2
	NLLS	**10.5496**	**3.248015**	**2.715038**	**10.00352**	**0.927626**	**1**
Sandia case 2	GA	10.62009	3.258848	2.721872	10.02281	0.927143	6
	PSO	10.62008	3.258847	2.721906	10.0228	0.927143	5
	NLLS	10.62008	3.258847	2.721906	10.0228	0.927143	4
Faiman	literature	39.29602	6.268654	5.23579	17.29068	0.731097	17
Faiman case 0	NLLS	15.57204	3.946142	3.185333	11.15458	0.893171	16
Faiman case 1	GA	10.62118	3.259015	2.72547	10.03256	0.927135	9
	PSO	10.62117	3.259014	2.72551	10.03269	0.927135	8
	NLLS	10.62117	3.259014	2.72551	10.03269	0.927135	7
Faiman case 2	GA	10.69227	3.269904	2.732557	10.05253	0.926647	12
	PSO	10.69224	3.2699	2.732496	10.0523	0.926648	11
	NLLS	10.69224	3.2699	2.732497	10.0523	0.926648	10
Polynomial Regression		11.26802	3.356788	2.85461	10.06245	0.922698	13

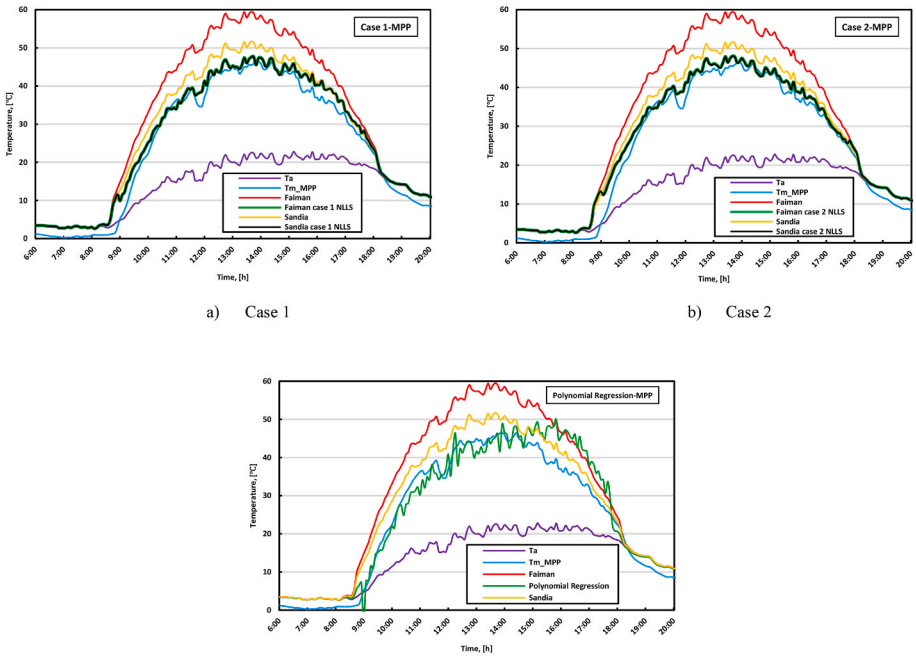

a) Case 1 b) Case 2

c) Polynomial Regression-MPP

Fig. 7. Calculated PV module temperature operating at MPP condition using various thermal models cases integrated with the EOS; a) Case 1; b) Case 2; and c) Polynomial Regression-MPP.

temperature prediction under MPP operation, evaluating the modified thermal models cases with EOS sensitivity.

When calculating the module temperature based on the meteorological variables presented in Fig. 7, the Faiman model notably overestimates the MPP module temperature. It yielded a calculated module temperature of 46.32 °C, which is 29.27 % higher than the measured value. In contrast, the Sandia model, utilizing the literature's coefficients, showed better accuracy in predicting daily MPP module temperature. Its daily average module temperature was 40.37 °C, representing a 12.67 % overestimation compared to the measured temperature, as shown in Fig. 8. It is important to note that for the same conditions, the optimized coefficients for both the modified Faiman and Sandia thermal models resulted in nearly identical estimations using the same meteorological variables.

The modified Faiman model in case 1 calculated the MPP operating module temperature as 37.67 °C, which overestimates the measured value by 5.19 %. Notably, both the Faiman and Sandia modified models in case 1 and 2 consistently exhibited the similar accuracy in estimating the MPP operated PV module temperature with error of 4.75 %–5.19 % which is significantly improved compared to the literature models, as

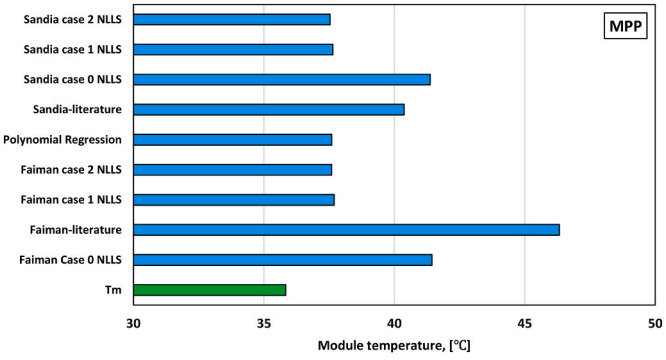

Fig. 8. Daily average module temperature of PV operating at MPP condition using various thermal models examined for 11th of March.

depicted in Fig. 9. Specifically, the Sandia model in case 1, optimized with NLLS, showed a MSE of 9.728 °C^2 and an R^2 of 0.9126. This represents an improvement of approximately 37.52 % and 6.65 % respectively, relative to the unoptimized Sandia model's prediction. Furthermore, the significant overestimation by the literature-derived Faiman model (MSE of 64.58 °C^2 and R^2 of 0.4198) was dramatically improved in the modified Faiman model case 1 with NLLS optimization, which achieved an MSE of 9.770 °C^2 and an R^2 of 0.911, as evident in Fig. 9(b).

Conversely, the Sandia model case 2 yielded a daily average module temperature of 37.53 °C (see Fig. 8), 1.70 °C higher than the measured daily average. Additionally, the polynomial regression thermal model, sensitive to EOS, calculated a daily average module temperature of 37.60 °C, which overestimates the measured temperature by 4.93 %. This is considered an acceptable accuracy improvement relative to commonly used thermal models in the literature. The significantly improved accuracy across these cases confirms the critical importance of integrating EOS into PV module thermal modelling. Overall, newly modified cases 1 and 2 demonstrated the best performance in estimating the module temperature of MPP-operated systems. Integrating the electrical efficiency in case 2 to estimate the module temperature operating at MPP has a minimum influence on the accuracy performance of both Sandia and Faiman model. On the other hand, case 1 of both Faiman and Sandia model shows a better prediction accuracy at low irradiance levels as can be noticed in Fig. 7.

4.4. *Thermal models evaluation for open-circuited PV modules*

Fig. 10 presents a performance comparison of various thermal models in estimating the temperature of an open-circuited PV module, considering three cases that incorporate the EOS into the models. While the traditional Faiman and Sandia models do not account for the module's electrical operating conditions, they predict the average daily temperature of the open-circuited PV module as 40.37 °C and 46.32 °C, showing a significant discrepancy relative to the measured open-circuited PV module temperature, achieving an average of 41.83 °C. it has been witnessed that both cases of each model; Faiman and Sandia

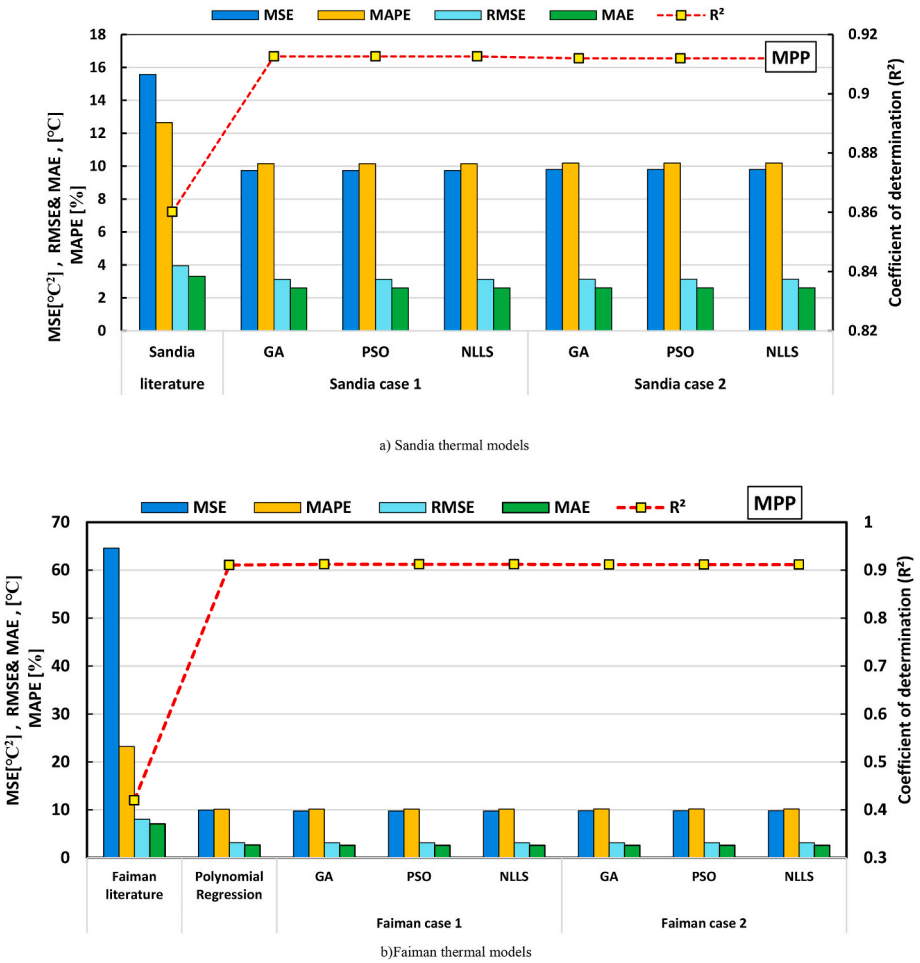

Fig. 9. Error statistics of different thermal models integrated with the EOS for calculating the module temperature of PV-MPP considering both; a) sandia thermal models; b)Faiman thermal models.

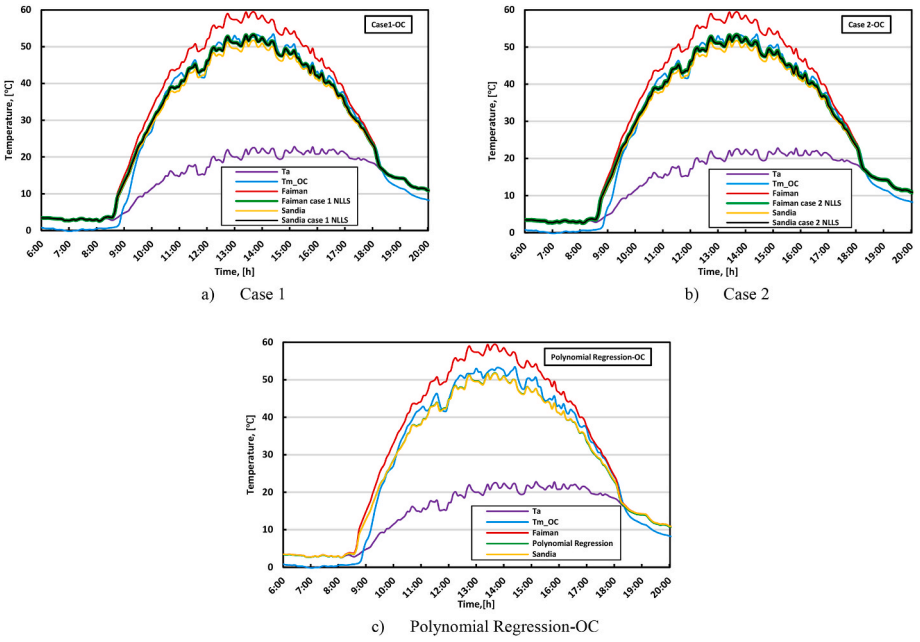

Fig. 10. Calculated PV module temperature operating at OC condition using various thermal models cases integrated with the EOS; a) Case 1; b) Case 2; and c) Polynomial Regression-OC.

models, have identical prediction performance. Operation under open-circuit conditions results in no power extraction and no current flow; therefore, $\eta_e = 0$ and EOS = $(I/I_{mpp}) = 0$. Accordingly, when the main coefficients of the thermal models are fixed, both cases are identical as can be seen in Fig. 10. When considering case 1 and case 2 of both modified Sandia and Faiman models, the daily average temperatures predicted are 41.537 °C and 41.47 °C, respectively, as shown in Fig. 11.

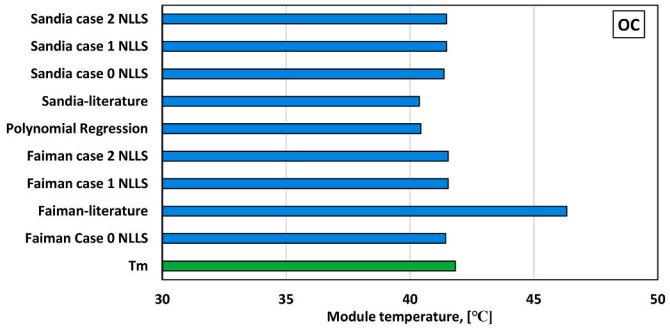

Fig. 11. Daily average module temperature of PV operating at OC condition using various thermal models examined for 11th of March.

While case 2 for these modified models achieved an daily average value of 41.35 °C and 41.41 °C respectively. Accordingly, the tuned coefficients in the modified Faiman and Sandia models lead to improved accuracy, reducing the prediction error from −3.85 % and 10.74 % (typical models) to 0.70 % and 0.86 %, respectively.

Furthermore, as seen in Fig. 12, the error statistics of the Sandia model improved with EOS integration. The MSE decreased from 10.22 °C^2 (typical model) to 9.81°C^2 (Case 1&2), while the R^2 increased from 0.928 to 0.931. Similarly, the Faiman model showed significant improvement, with MSE reduced from 34.40 °C^2–9.90 °C^2—representing a 71.11 % reduction—and R^2 increasing from 0.759 to 0.930, an improvement of 22.55 %. Additionally, the Polynomial Regression thermal model slightly underestimates the module temperature during the day, as seen in Fig. 10(d). It yields an average daily module temperature of 40.43 °C, which is 3.33 % lower than the actual measured value.

4.5. Thermal models evaluation for short-circuited PV modules

Fig. 13 shows the prediction performance of the thermal models in calculating the module temperature of a short-circuited PV module throughout the day. While the typical Faiman model is known to significantly overestimate the module temperature under maximum power point and open-circuit conditions, its performance improves

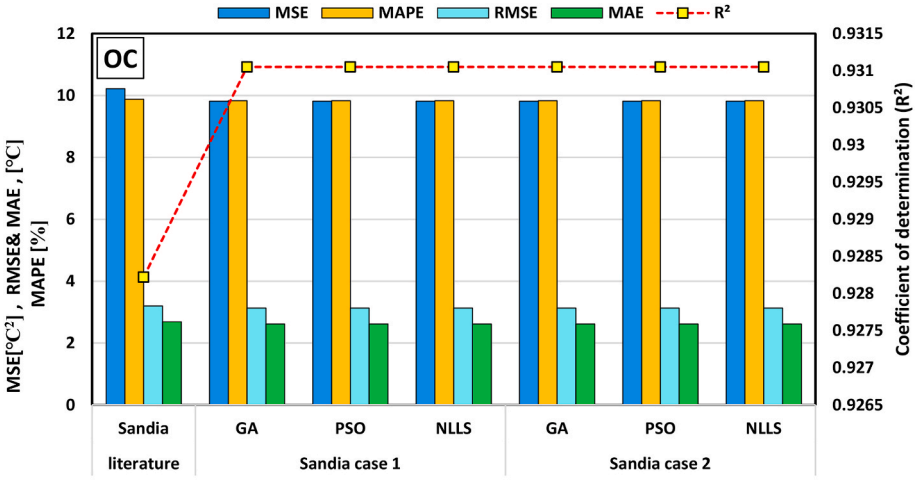

a) Sandia thermal models

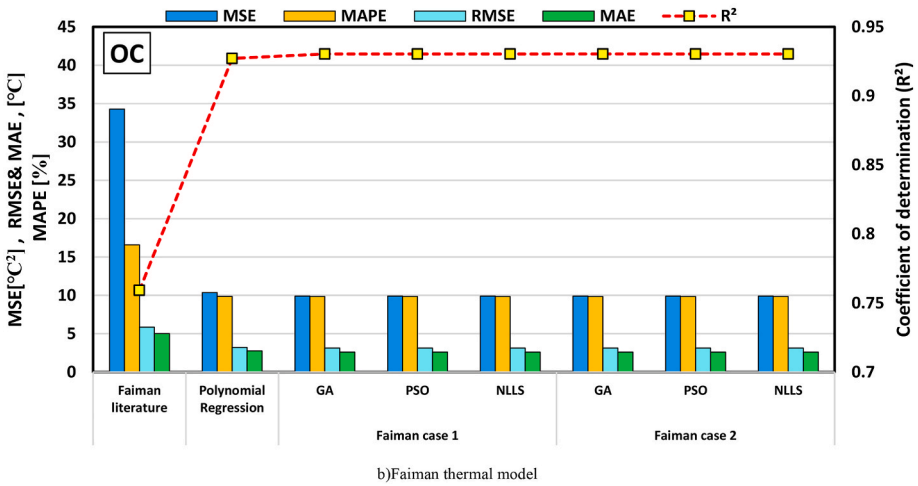

b)Faiman thermal model

Fig. 12. Error statistics of different thermal models integrated with the EOS for calculating the module temperature of PV-OC considering both; a) Sandia thermal models; b) Faiman thermal models.

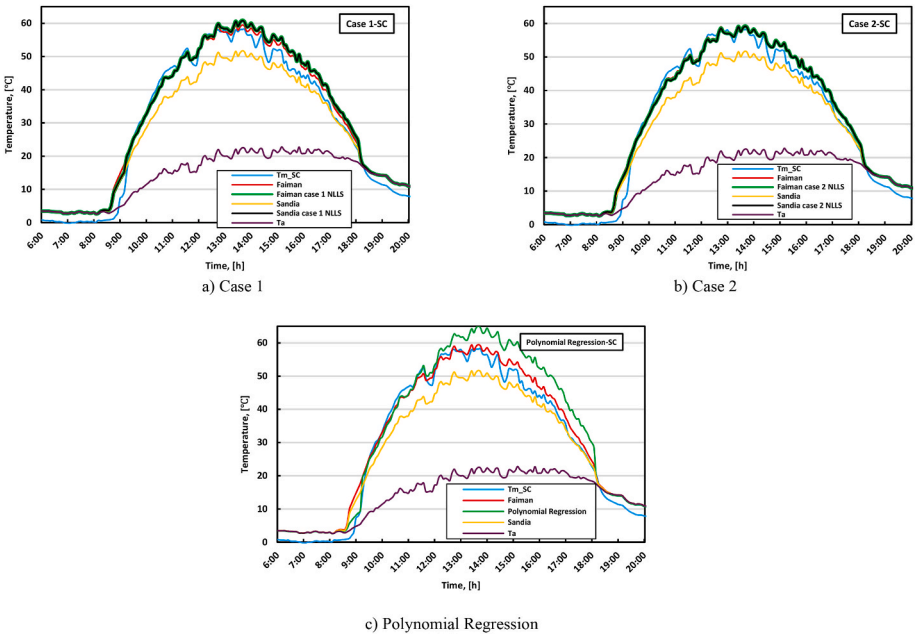

Fig. 13. Calculated PV module temperature operating at SC condition using various thermal models cases integrated with the EOS; a) Case 1; b) Case 2; and c) Polynomial Regression.

under short-circuit conditions. As shown in Fig. 13, the typical Faiman model predicts a daily average temperature of 46.32 °C for the short-circuited module, overestimating the measured value by only 2.74 %.

Enhancing the mathematical formulations by integrating the EOS as an input, as done in cases 1 and 2, led to notable improvements in predicting the temperature of the short-circuited PV module, as evidenced in Fig. 13(b) and (c). Moreover, it can be noticed that both modified Sandia and Faiman models slightly overestimate the module temperature—especially during afternoon hours post solar noon 13:00 p.m. Using NLLS optimization, the predicted daily average temperatures for modified Faiman models, cases 1 and 2, were 47.05 °C and 46.99 °C, respectively, as can be seen in Fig. 14. While both cases 1 and case 2 of the modified Sandia models have an average module temperature of 46.97 °C and 45.91 °C, respectively. This means that integrating EOS into both Faiman and Sandia models improves the prediction accuracy to >1 °C compared to the literature ones that have +2.74 % (for Faiman-literature) and −10.45 % (for Sandia-literature). This minimal deviation confirms the improved accuracy and robustness of the Case 2 formulations for both the Sandia and Faiman models.

The error statistics for the NLLS-optimized modified Sandia Case 2 model also reflect this improvement, with a MSE of 12.24 $°C^2$ and a coefficient of determination R^2 of 0.929, compared to an MSE of 21.58 $°C^2$ and R^2 of 0.875 for the typical Sandia model, see Fig. 15. It is worth noting that the elevated error metrics are largely attributable to the model's overestimation of temperature in the late afternoon, combined with the presence of some cloudy hours in the dataset, which may have affected the thermal dynamics and reduced prediction accuracy. The Polynomial Regression thermal model consistently overestimates the SC module temperature after the solar noon, as shown in Fig. 13(c). It predicts a daily average temperature of 49.52 °C, which is 9.58 % higher than the measured value. Nonetheless, the Polynomial Regression thermal model achieves an MSE of 18.73 $°C^2$ and an R^2 of 0.922, indicating an acceptable overall prediction performance despite the slight overestimation.

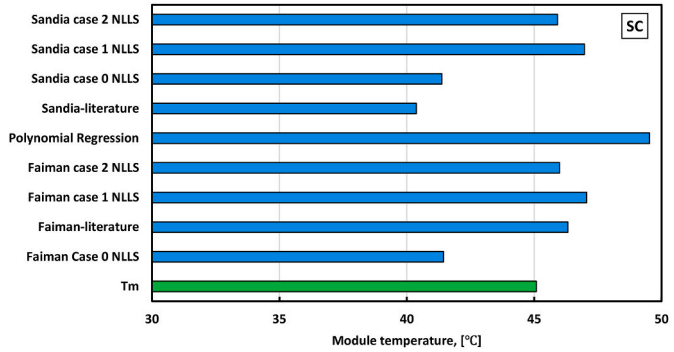

Fig. 14. Daily average module temperature of PV operating at SC condition using various thermal models examined for 11th of March.

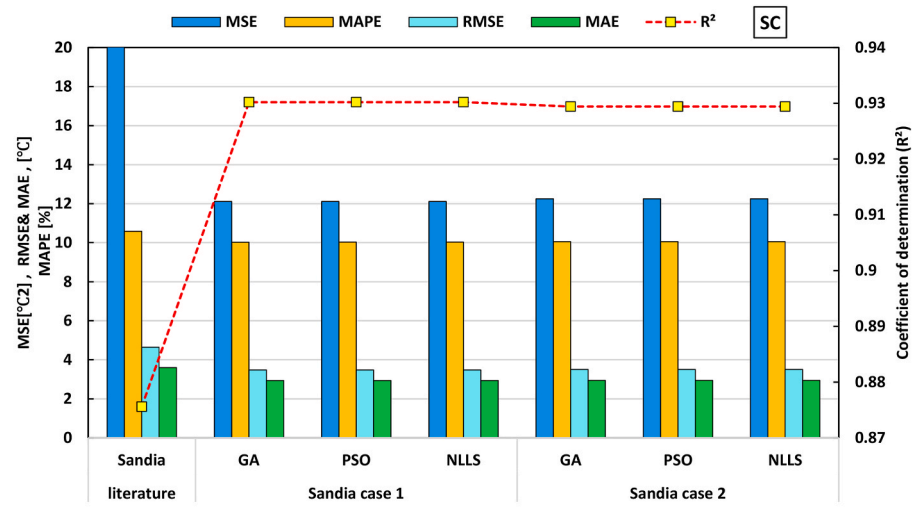

a) Sandia thermal models

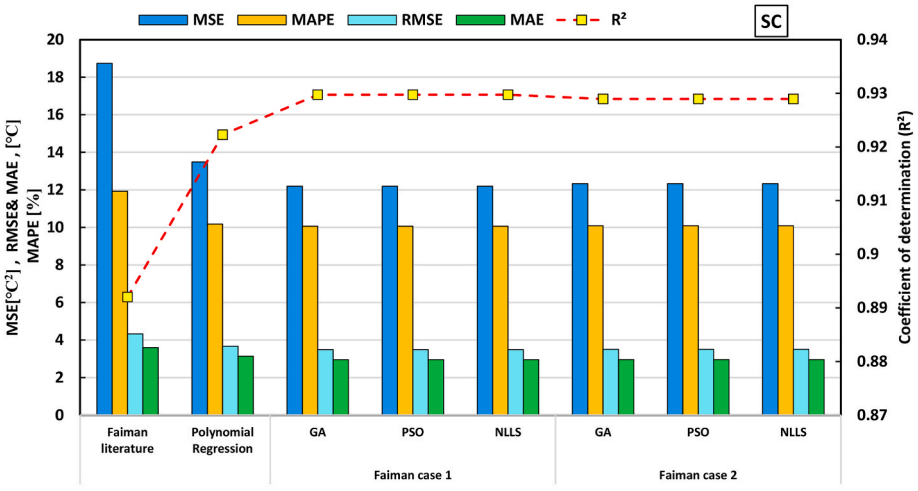

b) Faiman thermal models

Fig. 15. Error statistics of different thermal models integrated with the EOS for calculating the module temperature of PV-SC, considering both; a) Sandia thermal models; b)Faiman thermal models.

5. Conclusion

This study introduced the concept of integrating the sensitivity of the electrical operating status (EOS) of photovoltaic (PV) modules into thermal modeling to enhance accuracy. Modifications were applied to two widely used thermal models—the Faiman and Sandia models—by incorporating the ratio between the measured and calculated current at the maximum power point (MPP) under given meteorological conditions as an additional input. This integration was implemented through two different parabolic formulations, one of which includes the electrical efficiency. Furthermore, a polynomial regression-based thermal model was developed for deeper investigation.

To achieve the research objectives, three identical PV systems were operated simultaneously under different EOS conditions over four months. PV Set 1 and PV Set 2 were operated under short-circuit and open-circuit conditions, respectively, while PV Set 3 was operated at MPP. Three optimization algorithms were employed to estimate the coefficients for each case and each modified model.

The following conclusions were drawn:

- Integrating EOS sensitivity into thermal models significantly improved the accuracy of module temperature predictions compared to conventional models from the literature.
- For each case, the modified Sandia and Faiman models demonstrated nearly identical prediction performance, regardless of the optimization algorithm used (Genetic Algorithm, Particle Swarm Optimization, or Non-Linear Least Squares).
- The EOS integration in Case 1 yielded the most promising results across the examined EOS. The modified Sandia model, optimized using the Non-Linear Least Squares algorithm, achieved the highest overall accuracy with an R^2 of 0.9276, MSE of 10.549 $°C^2$, and RMSE of 3.248 °C. This outperformed the typical Sandia model (R^2 = 0.897, MSE = 15.028 $°C^2$, RMSE = 3.876 °C) and the Faiman model (R^2 = 0.731, MSE = 39.296 $°C^2$, RMSE = 6.268 °C).
- The modified Faiman model (Case 1) optimized with NLLS, estimated the MPP module temperature as 37.594 °C, deviating by less than 4.91 % from the measured value. It achieved an MSE of 9.845 $°C^2$ and R^2 of 0.9115, whereas the literature-based Faiman model significantly overestimated the temperature with an MSE of 64.586 °C and R^2 of 0.4199.
- For the open-circuited module, both modified cases of Faiman and Sandia have nearly identical predictions, with only a 0.70 % and 0.86 % underestimation compared to a +10.74 % and 3.48 % error while considering the conventional model, respectively.
- With NLLS, the predicted daily average temperature of the short-circuited PV module (Case 2) was 45.91 °C—only 0.829 °C higher

than the measured value. This minimal deviation confirms the improved accuracy and robustness of the case 2 formulations in both the Sandia and Faiman models in estimating the module temperature that operates at short-circuit conditions. Error statistics further validate this enhancement, with the case 2 model achieving an MSE of 12.249 °C and R^2 of 0.9294, compared to an MSE of 21.58 °C and R^2 of 0.8755 for the typical Sandia model.

The current study focused on three key reference EOS—OC, MPP, and SC—to evaluate the impact of EOS sensitivity on PV module thermal behavior. While these cases capture the typical bounds of PV operation, real-world systems often operate under partial shading, inverter clipping, or curtailment, leading to derated power conditions that deviate from these standard reference points. Future work will therefore aim to investigate a broader range of EOS scenarios, including intermediate and dynamically changing conditions, to further refine the proposed thermal models. This will facilitate a deeper understanding of PV module thermal responses under realistic field conditions and support the development of more accurate and adaptive thermal modeling frameworks for both performance monitoring and energy yield forecasting.

CRediT authorship contribution statement

Giuseppe Marco Tina: Writing – review & editing, Validation, Supervision, Project administration, Methodology, Investigation, Funding acquisition, Formal analysis, Data curation, Conceptualization, Resources. **Amr Osama:** Writing – review & editing, Writing – original draft, Visualization, Validation, Software, Methodology, Investigation, Formal analysis, Data curation, Conceptualization. **Antonio Gagliano:** Writing – review & editing, Validation, Supervision, Methodology, Formal analysis, Conceptualization, Data curation, Writing – original draft. **Gaetano Mannino:** Writing – review & editing, Validation, Methodology, Investigation, Formal analysis, Conceptualization, Data curation, Software. **Francisco José Munoz-Rodríguez:** Writing – review & editing, Visualization, Validation, Resources, Methodology, Funding acquisition, Formal analysis, Conceptualization, Supervision, Project administration. **Gabino Jiménez-Castillo:** Writing – review & editing, Writing – original draft, Validation, Supervision, Software, Methodology, Investigation, Formal analysis, Data curation, Conceptualization, Funding acquisition, Resources.

Declaration of competing interest

The authors declare that they have no known competing financial interests or personal relationships that could have appeared to influence the work reported in this paper.

Acknowledgment

This work has been supported by the Italian National Ph.D. in Photovoltaics, CURRICULUM C: Monitoring and Diagnosis has been received (CUP: D42B22001610006). Also, supported by MUR, Italy funds in the frame of PRIN 2020 “A Holistic Monitoring and Diagnostic Tool for Photovoltaic Generators (HOTSPHOT)” project (CUP: E63C2001116000) and Grant TED2021-131137B-I00 “Aportación a la Transición Ecológica en el sector Industrial a través del Autoconsumo Fotovoltaico” funded by MICIU/AEI/10.13039/501100011033 and European Union Next Generation EU/PRTR.

Data availability

Data will be made available on request.

References

[1] International Energy Agency (IEA), Active Power Management of Photovoltaic Systems - State of the Art and Technical Solutions 2024, 2024.
[2] B. Sambasivam, Y. Xu, Reducing solar PV curtailment through demand-side management and economic dispatch in Karnataka, India, Energy Policy 172 (2023) 113334, https://doi.org/10.1016/j.enpol.2022.113334.
[3] J.M. Riquelme-Dominguez, S. Martinez, A photovoltaic power curtailment method for operation on both sides of the power-voltage curve, Energies (Basel) 13 (15) (2020), https://doi.org/10.3390/en13153906.
[4] B. Limane, C. Ould-Lahoucine, S. Diaf, Modeling and simulation of the thermal behavior and electrical performance of PV modules under different environment and operating conditions, Renew. Energy 219 (P1) (2023) 119420, https://doi.org/10.1016/j.renene.2023.119420.
[5] L. Ghabuzyan, K. Pan, A. Fatahi, J. Kuo, C. Baldus-Jeursen, Thermal effects on photovoltaic array performance: experimentation, modeling, and simulation, Appl. Sci. (Switzerland) 11 (4) (2021) 1–15, https://doi.org/10.3390/app11041460.
[6] Y.Y. Hong, R.A. Pula, Methods of photovoltaic fault detection and classification: a review, Energy Rep. 8 (2022) 5898–5929, https://doi.org/10.1016/j.egyr.2022.04.043.
[7] Y.K. Singh, S. Dubey, P. Rajput, K.Y. Singh, K. Pandey, Real-time and modelled performance assessment and validation studies of PV modules operating in varied climatic zones, Energ. Built Environ. (November 2023, 2024), https://doi.org/10.1016/j.enbenv.2023.11.009.
[8] M.A. Djeziri, S. Benmoussa, R.T. Sanshez, O. Palais, G.M. Tina, Solar cell modeling in normal and degraded operations for simulation and monitoring, Sustain. Energy Technol. Assessments 51 (August 2021) 101990, https://doi.org/10.1016/j.seta.2022.101990, 2022.
[9] M. Perez, R. Perez, K.R. Rábago, M. Putnam, Overbuilding & curtailment: the cost-effective enablers of firm PV generation, Sol. Energy 180 (2019) 412–422, https://doi.org/10.1016/j.solener.2018.12.074.
[10] M.J. Perez, R. Perez, T.E. Hoff, Ultra-high photovoltaic penetration: where to deploy, Sol. Energy 224 (2021) 1079–1098, https://doi.org/10.1016/j.solener.2021.06.041.
[11] M. Pierro, R. Perez, M. Perez, M.G. Prina, D. Moser, C. Cornaro, Italian protocol for massive solar integration: from solar imbalance regulation to firm 24/365 solar generation, Renew. Energy 169 (2021) 425–436, https://doi.org/10.1016/j.renene.2021.01.023.
[12] PV magazine - Photovoltaics markets and technology, Trina Solar sets world record for solar module efficiency at 25.44%.” [Online]. Available: https://www.pv-magazine.com/2025/01/07/trina-solar-sets-world-record-for-solar-module-efficiency-at-25-44/.
[13] S.P. Aly, J.J. John, G. Mathiak, O. Albadwawi, L. Pomares, V. Alberts, A thermal model for bifacial PV panels, in: Conference Record of the IEEE Photovoltaic Specialists Conference, 2022-June, pp. 457–459, https://doi.org/10.1109/PVSC48317.2022.9938549, 2. 2022.
[14] S. Pereira, P. Canhoto, T. Oozeki, R. Salgado, Assessment of thermal modeling of photovoltaic panels for predicting power generation using only manufacturer data, Energy Rep. 12 (May) (2024) 1431–1448, https://doi.org/10.1016/j.egyr.2024.07.039.
[15] A. Gholami, M. Ameri, M. Zandi, R.G. Ghoachani, Electrical , thermal and optical modeling of photovoltaic systems : step-by-Step guide and comparative review study, Sustain. Energy Technol. Assessments 49 (June 2021) (2022) 101711, https://doi.org/10.1016/j.seta.2021.101711.
[16] A.Q. Jakhrani, A.K. Othman, A.R.H. Rigit, S.R. Samo, Determination and comparison of different photovoltaic module temperature models for Kuching, Sarawak. 2011 IEEE 1st Conference on Clean Energy and Technology, CET 2011, 2011, pp. 231–236, https://doi.org/10.1109/CET.2011.6041469.
[17] G.M. Tina, F.B. Scavo, A. Gagliano, Multilayer thermal model for evaluating the performances of monofacial and bifacial photovoltaic modules, IEEE J. Photovoltaics 10 (4) (2020) 1035–1043.
[18] C. Li, S.V. Spataru, K. Zhang, Y. Yang, H. Wei, A multi-state dynamic thermal model for accurate photovoltaic cell temperature estimation, IEEE J. Photovoltaics 10 (5) (2020) 1465–1473, https://doi.org/10.1109/JPHOTOV.2020.2987401.
[19] Z. Zhang, et al., The mathematical and experimental analysis on the steady-state operating temperature of bifacial photovoltaic modules, Renew. Energy 155 (2020) 658–668, https://doi.org/10.1016/j.renene.2020.03.121.
[20] B. Tuncel, T. Ozden, R.S. Balog, B.G. Akinoglu, Dynamic thermal modelling of PV performance and effect of heat capacity on the module temperature, Case Stud. Therm. Eng. 22 (September) (2020) 100754, https://doi.org/10.1016/j.csite.2020.100754.
[21] R. Korab, M. Połomski, T. Naczyński, T. Kandzia, A dynamic thermal model for a photovoltaic module under varying atmospheric conditions, Energy Convers. Manag. 280 (October 2022) 116773, https://doi.org/10.1016/j.enconman.2023.116773, 2023.
[22] G. Tina, A coupled electrical and thermal model for photovoltaic modules, J. Solar Energy Eng. Transact. ASME 132 (2) (May 2010) 245011–245015, https://doi.org/10.1115/1.4001149.
[23] W. Gu, T. Ma, L. Shen, M. Li, Y. Zhang, W. Zhang, Coupled electrical-thermal modelling of photovoltaic modules under dynamic conditions, Energy 188 (Dec. 2019), https://doi.org/10.1016/j.energy.2019.116043.
[24] W. Gu, T. Ma, M. Li, L. Shen, Y. Zhang, A coupled optical-electrical-thermal model of the bifacial photovoltaic module, Appl. Energy 258 (August 2019) (2020) 114075, https://doi.org/10.1016/j.apenergy.2019.114075.

[25] R. Aalloul, R. Adhiri, M. Benlattar, A. Elaissaoui, Coupled electrical–thermal Modeling of Photovoltaic Modules: an Overview, Elsevier Ltd., Oct. 01, 2024, https://doi.org/10.1016/j.tsep.2024.102962.
[26] D. Klimenta, D. Minić, L. Pantić-Ranđelović, I. Radonjić-Mitić, M. Premović-Zečević, Modeling of steady-state heat transfer through various photovoltaic floor laminates, Appl. Therm. Eng. 229 (December 2022) (2023), https://doi.org/10.1016/j.applthermaleng.2023.120589.
[27] A. Yigit, N. Arslanoglu, H. Gul, Transient thermal modeling and performance analysis of photovoltaic panels, Environ. Prog. Sustain. Energy (2022), https://doi.org/10.1002/ep.14052.
[28] E. Barykina, A. Hammer, Modeling of photovoltaic module temperature using Faiman model: sensitivity analysis for different climates, Sol. Energy 146 (2017) 401–416, https://doi.org/10.1016/j.solener.2017.03.002.
[29] D.L. King, W.E. Boyson, J.A. Kratochvil, "Photovoltaic array performance model, SANDIA Report SAND2004-3535 8 (December) (2004) 1–19. Sandia Report No. 2004-3535.
[30] F.P. Arrays, A Simplified Thermal Model for Flat-Plate Photovoltic Array, 1987.
[31] E. Skoplaki, A.G. Boudouvis, J.A. Palyvos, A simple correlation for the operating temperature of photovoltaic modules of arbitrary mounting, Sol. Energy Mater. Sol. Cell. 92 (11) (2008) 1393–1402, https://doi.org/10.1016/j.solmat.2008.05.016.
[32] M. Zouine, et al., Mathematical models calculating PV module temperature using weather data: experimental study, Lecture Notes Electr. Eng. 519 (April) (2019) 630–639, https://doi.org/10.1007/978-981-13-1405-6_72.
[33] R. Kumar, C.S. Rajoria, A. Sharma, S. Suhag, Design and simulation of standalone solar PV system using PVsyst Software: a case study, Mater. Today Proc. 46 (2020) 5322–5328, https://doi.org/10.1016/j.matpr.2020.08.785.
[34] J.L.D.S. Silva, T.S. Costa, K.B. De Melo, E.Y. Sako, H.S. Moreira, M.G. Villalva, A comparative performance of PV power simulation software with an installed PV plant, Proc. IEEE Int. Conf. Indus. Technol. 2020-Febru (2020) 531–535, https://doi.org/10.1109/ICIT45562.2020.9067138.
[35] T.W. Neises, S.A. Klein, D.T. Reindl, Development of a thermal model for photovoltaic modules and analysis of NOCT guidelines, J. Solar Energy Eng. Transact. ASME 134 (1) (2012) 1–7, https://doi.org/10.1115/1.4005340.
[36] B. Herteleer, A. Kladas, G. Chowdhury, F. Catthoor, J. Cappelle, Investigating methods to improve photovoltaic thermal models at second-to-minute timescales, Sol. Energy 263 (August) (2023), https://doi.org/10.1016/j.solener.2023.111889.
[37] D. Wang, Z. Liang, Z. Zhang, M. Li, Efficient estimation of convective cooling of photovoltaic arrays: a physics-informed machine learning approach, Energ. AI 20 (2025) 100499, https://doi.org/10.1016/j.egyai.2025.100499.
[38] A.K. Podder, N.K. Roy, H.R. Pota, MPPT methods for solar PV systems: a critical review based on tracking nature, IET Renew. Power Gener. 13 (10) (2019) 1615–1632, https://doi.org/10.1049/iet-rpg.2018.5946.
[39] T. Neumann and I. Erlich, "Short Circuit Current Contribution of a Photovoltaic Power Plant", doi: 10.3182/20120902-4-FR-2032.00061. .
[40] S. Yuan, B.F. Yang, J.Y. Zhang, Experimental study on short-circuit current characteristics of a photovoltaic system with low voltage ride through capability under a symmetrical fault, Energy Rep. 8 (2022) 4502–4511, https://doi.org/10.1016/j.egyr.2022.03.089.
[41] M. Boussaid, A. Belghachi, K. Agroui, M. Abdelaoui, M. Otmani, Solar cell degradation under open circuit condition in out-doors-in desert region, Results Phys. 6 (2016) 837–842, https://doi.org/10.1016/j.rinp.2016.09.013.
[42] J. Kenfack, D. Kassegne, F. Menga, S.S. Ouro-djobo, Faults in a Photovoltaic System, 2023.
[43] A. Osama, G.M. Tina, A. Gagliano, Thermal models for mono/bifacial modules in ground/floating photovoltaic systems: a review, Renew. Sustain. Energy Rev. 216 (2025) 115627, https://doi.org/10.1016/j.rser.2025.115627. March.
[44] E. Skoplaki, J.A. Palyvos, Operating temperature of photovoltaic modules: a survey of pertinent correlations, Renew. Energy 34 (1) (2009) 23–29, https://doi.org/10.1016/j.renene.2008.04.009.
[45] A. Osama, G.M. Tina, A. Gagliano, G. Jimenez-Castillo, F.J. Munoz-Rodríguez, Effect of electrical operating conditions on thermal behavior of PV modules: numerical and experimental analysis, Sol. Energy Mater. Sol. Cell. 287 (April, 2025), https://doi.org/10.1016/j.solmat.2025.113625.
[46] D. Faiman, Assessing the outdoor operating temperature of photovoltaic modules, Prog. Photovoltaics Res. Appl. 16 (4) (Jun. 2008) 307–315, https://doi.org/10.1002/pip.813.
[47] IEC 61853-2:2016 | IEC photovoltaic (PV) module performance testing and energy rating - part 2: spectral responsivity, incidence angle and module operating temperature measurements. https://webstore.iec.ch/publication/25811#additionalinfo. (Accessed 12 August 2023).
[48] N. Martín-Chivelet, J. Polo, C. Sanz-Saiz, L.T. Núñez Benítez, M. Alonso-Abella, J. Cuenca, Assessment of PV module temperature models for building-integrated photovoltaics (BIPV), Sustainability 14 (3) (2022) 1–15, https://doi.org/10.3390/su14031500.
[49] A. Osama, G.M. Tina, G. Mannino, A.V. Cucuzza, A. Canino, F. Bizzarri, Experimental and Simulated Performance Evaluation of Bifacial Photovoltaic Floating System With a Horizontal Single-Axial Tracker, IEEE J Photovolt (2025). https://doi.org/10.1109/JPHOTOV.2025.3551505.
[50] A. Driesse, M. Theristis, J.S. Stein, PV module operating temperature model equivalence and parameter translation, in: Conference Record of the IEEE Photovoltaic Specialists Conference, 2022-June, pp. 172–177, https://doi.org/10.1109/PVSC48317.2022.9938895, 4. 2022.
[51] M. Koehl, M. Heck, S. Wiesmeier, J. Wirth, Modeling of the nominal operating cell temperature based on outdoor weathering, Sol. Energy Mater. Sol. Cell. 95 (7) (2011) 1638–1646, https://doi.org/10.1016/j.solmat.2011.01.020.
[52] G. Tina, F. Bontempo, L. Merlo, F. Bizzarri, Comparative analysis of monofacial and bifacial photovoltaic modules for floating power plants, Appl. Energy 281 (October 2020) 116084, https://doi.org/10.1016/j.apenergy.2020.116084, 2021.
[53] G.M. Tina, A. Osama, G. Mannino, A. Gagliano, A.V. Cucuzza, F. Bizzarri, Thermal comparison of floating bifacial and monofacial photovoltaic modules considering two laying configurations, Appl. Energy 389 (December 2024) (2025) 125732, https://doi.org/10.1016/j.apenergy.2025.125732.
[54] A. Idzkowski, K. Karasowska, W. Walendziuk, Temperature analysis of the stand-alone and building integrated photovoltaic systems based on simulation and measurement data, Energies (Basel) 13 (6) (2020), https://doi.org/10.3390/en13164274.
[55] D.L. King, W.E. Boyson, J.A. Kratochvil, Photovoltaic array performance model, Sandia Rep. No. 2004-3535 8 (2004) 1–19, https://doi.org/10.2172/919131. December.
[56] A. Keddouda, R. Ihaddadene, A. Boukhari, A. Atia, Experimental and numerical modeling of photovoltaic modules temperature under varying ambient conditions, Energy Convers. Manag. 312 (May) (2024) 118563, https://doi.org/10.1016/j.enconman.2024.118563.
[57] L. de O. Santos, P.C.M. de Carvalho, C. de O.C. Filho, Photovoltaic cell operating temperature models: a review of correlations and parameters, IEEE J. Photovoltaics 12 (1) (2022) 179–190, https://doi.org/10.1109/JPHOTOV.2021.3113156.
[58] J.M. Servant, CALCULATION OF THE CELL TEMPERATURE FOR PHOTOVOLTAIC MODULES FROM CLIMATIC DATA, vol. 3, Jan. 1986, pp. 1640–1643, https://doi.org/10.1016/B978-0-08-033177-5.50311-2.
[59] M. Mattei, G. Notton, C. Cristofari, M. Muselli, P. Poggi, Calculation of the polycrystalline PV module temperature using a simple method of energy balance, Renew. Energy 31 (4) (Apr. 2006) 553–567, https://doi.org/10.1016/j.renene.2005.03.010.
[60] Y. Chaibi, A. Allouhi, M. Malvoni, M. Salhi, R. Saadani, Solar irradiance and temperature influence on the photovoltaic cell equivalent-circuit models, Sol. Energy 188 (January) (2019) 1102–1110, https://doi.org/10.1016/j.solener.2019.07.005.
[61] A. Luque, A. Martí, A. Bett, V.M. Andreev, C. Jaussaud, J.A.M. van Roosmalen, J. Alonso, A. Räuber, G. Strobl, W. Stolz, C. Algora, B. Bitnar, A. Gombert, C. Stanley, P. Wahnon, J.C. Conesa, W.G.J.H.M. van Sark, A. Meijerink, G.P.M. van Klink, K. Barnham, R. Danz, T. Meyer, I. Luque-Heredia, R. Kenny, C. Christofides, G. Sala, P. Benítez, FULLSPECTRUM: a new PV wave making more efficient use of the solar spectrum, Solar Energy Materials and Solar Cells 87 (2005) 467–479.
[62] E. Yandri, The effect of Joule heating to thermal performance of hybrid PVT collector during electricity generation, Renew. Energy 111 (2017) 344–352, https://doi.org/10.1016/j.renene.2017.03.094.
[63] H. Morchid, M. Conlon, Investigation of the Effects of Joule Heating on the Performance of Photovoltaic Modules, 2017.
[64] R. Kumar, R. Gupta, Shunts in Crystalline Silicon PV Modules: a Comprehensive Review of Investigation, Characterization, and Mitigation, Elsevier B.V., Oct. 15, 2024, https://doi.org/10.1016/j.solmat.2024.113121.
[65] M.J. Heredia-Rios, L. Hernandez-Martinez, M. Linares-Aranda, M. Moreno-Moreno, J.F. Méndez, Analysis of losses associated with series resistance (Rs) in simple-structured c-Si solar cells, Energies (Basel) 17 (7) (Apr. 2024), https://doi.org/10.3390/en17071520.
[66] P. Malik, S.S. Chandel, A new integrated single-diode solar cell model for photovoltaic power prediction with experimental validation under real outdoor conditions, Int. J. Energy Res. 45 (1) (Jan. 2021) 759–771, https://doi.org/10.1002/er.5881.
[67] A. Khorami, M. Joodaki, Extracting voltage-dependent series resistance of single diode model for organic solar cells, SN Appl. Sci. 1 (6) (Jun. 2019), https://doi.org/10.1007/s42452-019-0613-2.
[68] T.M. Mahim, A.H.M.A. Rahim, M.M. Rahman, Review of mono-and bifacial photovoltaic technologies: a comparative study, IEEE J. Photovoltaics 14 (3) (2024) 375–396, https://doi.org/10.1109/JPHOTOV.2024.3366698.
[69] T. Villemin, R. Claverie, J.-P. Sawicki, G. Parent, Thermal characterization of a photovoltaic panel under controlled conditions, Renew. Energy 198 (2022) 28–40, https://doi.org/10.1016/j.renene.2022.08.036.
[70] H. El Achouby, M. Zaimi, A. Ibral, E.M. Assaid, New analytical approach for modelling effects of temperature and irradiance on physical parameters of photovoltaic solar module, Energy Convers. Manag. 177 (July) (2018) 258–271, https://doi.org/10.1016/j.enconman.2018.09.054.
[71] C.F. Abe, J.B. Dias, G. Notton, P. Poggi, Computing solar irradiance and average temperature of photovoltaic modules from the maximum power point coordinates, IEEE J. Photovoltaics 10 (2) (2020) 655–663, https://doi.org/10.1109/JPHOTOV.2020.2966362.
[72] C.F. Abe, J.B. Dias, G. Notton, G.A. Faggianelli, Experimental application of methods to compute solar irradiance and cell temperature of photovoltaic modules, Sensors (Switzerland) 20 (9) (2020), https://doi.org/10.3390/s20092490.
[73] M. Agoundedemba, C.K. Kim, H.G. Kim, R. Nyenge, N. Musila, Modelling and optimization of microgrid with combined genetic algorithm and model predictive control of PV/Wind/FC/battery energy systems, Energy Rep. 13 (November 2024) 238–255, https://doi.org/10.1016/j.egyr.2024.12.008, 2025.
[74] D. Saadaoui, M. Elyaqouti, K. Assalaou, D. Ben hmamou, S. Lidaighbi, Parameters optimization of solar PV cell/module using genetic algorithm based on non-uniform mutation, Energy Convers. Manag. X 12 (November) (2021) 100129, https://doi.org/10.1016/j.ecmx.2021.100129.
[75] G. Espitia-Mesa, A. Moreno-Villa, S. Tobón-Echavarría, J.C. Rivera, R. Mejía-Gutiérrez, Modeling optimal PV surface of BIPVs for maximum energy yield through genetic algorithms, Energ. Built Environ. 6 (4) (2024) 607–615, https://doi.org/10.1016/j.enbenv.2024.01.010.

[76] K. Alexakis, V. Benekis, P. Kokkinakos, D. Askounis, Genetic algorithm-based multi-objective optimisation for energy-efficient building retrofitting: a systematic review, Energy Build. 328 (December 2024) (2025) 115216, https://doi.org/10.1016/j.enbuild.2024.115216.
[77] Y. Shaiek, M. Ben Smida, A. Sakly, M.F. Mimouni, Comparison between conventional methods and GA approach for maximum power point tracking of shaded solar PV generators, Sol. Energy 90 (2013) 107–122, https://doi.org/10.1016/j.solener.2013.01.005.
[78] L. Abualigah, A. Sheikhan, A.M. Ikotun, R.A. Zitar, A.R. Alsoud, I. Al-Shourbaji, A. G. Hussien, H. Jia, 1 - Particle swarm optimization algorithm: review and applications, in: L. Abualigah (Ed.), Metaheuristic Optimization Algorithms, Morgan Kaufmann, 2024, pp. 1–14. https://doi.org/10.1016/B978-0-443-13925-3.00019-4.
[79] C.D. Iweh, E.R. Akupan, Control and optimization of a hybrid solar PV – hydro power system for off-grid applications using particle swarm optimization (PSO) and differential evolution (DE), Energy Rep. 10 (2023) 4253–4270, https://doi.org/10.1016/j.egyr.2023.10.080. November.
[80] A.G. Gad, Particle swarm optimization algorithm and its applications: a systematic review, Springer 29 (5) (2022), https://doi.org/10.1007/s11831-021-09694-4. Netherlands.
[81] A. Singh, A. Sharma, S. Rajput, A. Bose, X. Hu, An investigation on hybrid particle swarm optimization algorithms for parameter optimization of PV cells, Electronics (Switzerland) 11 (6) (2022) 1–23, https://doi.org/10.3390/electronics11060909.
[82] J. Xu, Separable nonlinear least squares search of parameter values in photovoltaic models, IEEE J. Photovoltaics 12 (1) (2022) 372–380, https://doi.org/10.1109/JPHOTOV.2021.3126105.
[83] F. Javier Toledo, J.M. Blanes, V. Galiano, Two-step linear least-squares method for photovoltaic single-diode model parameters extraction, IEEE Trans. Ind. Electron. 65 (8) (2018) 6301–6308, https://doi.org/10.1109/TIE.2018.2793216.
[84] H. Oufettoul, N. Lamdihine, S. Motahhir, N. Lamrini, I.A. Abdelmoula, G. Aniba, Comparative performance analysis of PV module positions in a solar PV array under partial shading conditions, IEEE Access 11 (February 2023) 12176–12194, https://doi.org/10.1109/ACCESS.2023.3237250, 2023.
[85] N. Manoj Kumar, S. Chakraborty, S. Kumar Yadav, J. Singh, S.S. Chopra, Advancing simulation tools specific to floating solar photovoltaic systems – comparative analysis of field-measured and simulated energy performance, Sustain. Energy Technol. Assessments 52 (PB) (2022) 102168, https://doi.org/10.1016/j.seta.2022.102168.
[86] A. Osama, G.M. Tina, G. Mannino, A.V. Cucuzza, F. Bizzarri, Experimental and Numerical Performance Assessment of East-West Bifacial Photovoltaic Floating System in Freshwater Basins, IEEE Access (2024) 141425–141447. https://doi.org/10.1109/ACCESS.2024.3468228.
[88] G.M. Tina, G. Mannino, A. Osama, A. Cucuzza, A. Canino, F. Bizzarri, Floating Bifacial PV Systems: An Experimental Comparison. https://doi.org/10.23919/SpliTech65624.2025.11091615.
[90] N.A.S. Elminshawy, A. Ahmed, A. Osama, A.E. Kabeel, O. Elbaksawi, The potential of optimized floating photovoltaic system for energy production in the Northern Lakes of Egypt, Eng Anal Bound Elem 161 (2024) 226–246. https://doi.org/10.1016/j.enganabound.2024.01.022.